



## Research Papers

## Laser-induced graphitization (LIG) of a Mediterranean cultivation softwood: does anisotropy matter?

Alessio Mostaccio <sup>a</sup> , Francesco Bolognesi <sup>b,f</sup> , Valerio Appetito <sup>b</sup>, Joanna Filippi <sup>c</sup> , Leonardo Duranti <sup>d</sup> , Tilde De Caro <sup>e</sup> , Alessio Mezzi <sup>e</sup>, Francesca Romana Lamastra <sup>b</sup> , Daniela Caschera <sup>e</sup> , Giampiero Montesperelli <sup>b</sup> , Eugenio Martinelli <sup>c</sup> , Marco Togni <sup>f</sup> , Gaetano Marrocco <sup>a</sup> , Alessandra Bianco <sup>b,\*</sup>

<sup>a</sup> Università degli Studi di Roma "Tor Vergata", Dipartimento DICL, Via del Politecnico, 00133 Roma, Italy

<sup>b</sup> Università degli Studi di Roma "Tor Vergata", Dipartimento Ingegneria dell'Impresa "Mario Lucertini", Consortium INSTM UdR "Roma Tor Vergata", Via del Politecnico, 00133 Roma, Italy

<sup>c</sup> Università degli Studi di Roma "Tor Vergata", Dipartimento di Ingegneria Elettronica, Via del Politecnico, 00133 Roma, Italy

<sup>d</sup> Università degli Studi di Roma "Tor Vergata", Dipartimento di Scienze e Tecnologie Chimiche, Consortium INSTM UdR "Roma Tor Vergata", Via della Ricerca Scientifica, 00133 Roma, Italy

<sup>e</sup> Istituto per lo Studio dei Materiali Nanostrutturati ISMN-CNR, Strada Provinciale 35d/9, 00010 Montelibretti, Roma, Italy

<sup>f</sup> Università degli Studi di Firenze, Dipartimento di Scienze e Tecnologie Agrarie, Alimentari, Ambientali e Forestali (DAGR), Via San Bonaventura 13, Firenze, Italy



## ARTICLE INFO

## Keywords:

Green electronics

Laser induced graphitization

Softwood

Raman spectroscopy

Sheet resistance

## ABSTRACT

Laser-Induced Graphitization (LIG) is a cost-effective, scalable and versatile technique that allows the conversion of carbon-rich substrates into conductive carbonaceous layers, particularly promising in the field of printed electronics. Laser-Induced Graphitization of lignocellulosic materials (*green LIG*) represents an attractive choice for the development of sustainable zero-waste electronic and electrochemical devices. The focus of this study is on *Cedrus* sp. (cedar), a fast-growing cultivation softwood diffused in the Mediterranean area, mainly employed in arboriculture or processed in chips for biofuels. Cedar wood (dry density 0.47 g/cm<sup>3</sup>, longitudinal cut, minimum thickness 1 mm) was laser-scribed in room conditions using a conventional system. Laser power, defocusing and scribing direction have been systematically varied. Pristine and ant flame-treated wood substrates have been investigated. A comprehensive structural characterization was performed from the macro- to the nanoscale by optical microscopy, scanning electron microscopy, X-ray diffraction, X-ray photoelectron spectroscopy and Raman spectroscopy. The thermal degradation profiles were acquired by thermogravimetry and the electrical properties determined by four-point probe multimeter. Optimized LIG parameters (laser power 8 %, writing speed 1.75 %, minimum off-set 3 mm below the focal plane) led to the conversion of cedar wood into well-organized crack-free 3D carbonaceous layers characterized by a minimum sheet resistance of about 100 Ω/sq or 40 Ω/sq by single-run lasing, respectively, perpendicularly (cellulose-rich direction) or in parallel (lignin-rich direction) to the wood grain. LIG traces derived from wood pretreated with the ant flame showed comparable electrical performance (37 Ω/sq) if lased orthogonally to the wood grain (cellulose-rich direction), the Rs value increased by one order of magnitude (329 Ω/sq) lasing in parallel to the wood grain (lignin-rich direction). Therefore, this study revealed that the control of the laser-writing direction enables the optimization of the electrical performance of green LIG products derived from wood, also significantly contributing to the mitigate the variability of the results. The electrical properties of LIG traces derived from cedar wood in room conditions pave the way to the development of differential sensors, micro-fluidic devices and antennas for near-field communication.

\* Corresponding author.

E-mail addresses: [alessio.mostaccio@uniroma2.it](mailto:alessio.mostaccio@uniroma2.it) (A. Mostaccio), [francesco.bolognesi@uniroma2.it](mailto:francesco.bolognesi@uniroma2.it) (F. Bolognesi), [appetitovalerio@gmail.com](mailto:appetitovalerio@gmail.com) (V. Appetito), [filippi@ing.uniroma2.it](mailto:filippi@ing.uniroma2.it) (J. Filippi), [leonardo.duranti@uniroma2.it](mailto:leonardo.duranti@uniroma2.it) (L. Duranti), [tilde.decaro@cnr.it](mailto:tilde.decaro@cnr.it) (T. De Caro), [alessio.mezzi@cnr.it](mailto:alessio.mezzi@cnr.it) (A. Mezzi), [lamastra@scienze.uniroma2.it](mailto:lamastra@scienze.uniroma2.it) (F.R. Lamastra), [daniela.caschera@cnr.it](mailto:daniela.caschera@cnr.it) (D. Caschera), [montesperelli@stc.uniroma2.it](mailto:montesperelli@stc.uniroma2.it) (G. Montesperelli), [martinelli@ing.uniroma2.it](mailto:martinelli@ing.uniroma2.it) (E. Martinelli), [marco.togni@unifi.it](mailto:marco.togni@unifi.it) (M. Togni), [gaetano.marrocco@uniroma2.it](mailto:gaetano.marrocco@uniroma2.it) (G. Marrocco), [bianco@stc.uniroma2.it](mailto:bianco@stc.uniroma2.it) (A. Bianco).

<https://doi.org/10.1016/j.materresbull.2025.113460>

Received 7 January 2025; Received in revised form 27 March 2025; Accepted 31 March 2025

Available online 2 April 2025

0025-5408/© 2025 Elsevier Ltd. All rights reserved, including those for text and data mining, AI training, and similar technologies.

## 1. Introduction

*Green electronics* is one of the most promising areas of the undergoing sustainable transition. It represents a revolutionary perspective in the panorama of technological innovation, which focuses on the analysis and mitigation of the environmental impact generated by electronic products throughout the entire life cycle, from production to End of Life (EoL). The realization of eco-sustainable electronic devices is based on the integration of renewable and/or biodegradable materials, the limitation of the use of harmful substances in the production phase and the adoption of energy-efficient manufacturing processes [1]. The interest in biological materials as sustainable alternatives is growing, and the focus is currently on second generation biomass and fast-growing lignocellulosic species, aimed to develop low-cost technological products and devices [2–4].

*Laser-induced graphitization (LIG)* is considered a revolutionary technology in the field of conductive materials. The process is based on the irradiation of a target material by a laser beam, whose energy is partly absorbed and converted into thermal energy, while the remaining is reflected and/or diffused. By using pulsed laser radiation, natural and synthetic carbon-rich substrates are converted into a peculiar conductive 3D carbonaceous material [5,6]. The selection of process parameters is crucial to optimize the efficiency of the conversion and the properties of the product [7]. Natural and biologically-derived materials, as well as a wide range of polymeric materials, including polyimide (PI), polyetheretherketone (PEEK), and polysulfone (PSU), can be employed offering significant opportunities in the field of printable electronics and flexible devices [5,6,8]. LIG technique is extremely versatile and its applications in edible electronics [9], home automation [10], biosensors [11–15], electrochemical sensors [16–18], micro-fluidic sensors [19] and physical sensors for robotics, e-skin, healthcare and Internet of Things [20,21] are particularly appealing. Among the advantages offered by the LIG technique, the easily and simply patterning into desired shapes through computer-controlled design and the intrinsic integration between the substrate and the conductive layer that minimizes adhesion-related issues are distinguishable [5,6,8].

Recently, LIG materials derived from abundant and renewable organic bio-based substrates (e.g. wood, leaves, cork, husks, food) have been termed *green LIG (gLIG)* products [6].

Wood is the most widely used biological material, with almost 500 million cubic meters of sawnwood and 400 million cubic meters of plywood, particle board, and fibreboard used globally in 2018 [3]. The diversity of wood species found worldwide varies according to anatomical structures, wood chemistry, physical and mechanical properties. These variations support the broad classification of wood species into *hardwoods* and *softwoods*. Regardless of species, wood consists of three main components—cellulose, hemicellulose and lignin—that are assembled in a unique cellular structure that comprises the middle lamella, the primary cell wall and the secondary cell wall [22,23]. Cellulose accounts approximately for 40–45 % of the dry mass, in most wood species it is predominantly located in the secondary cell wall. Cellulose is linear high-molecular-weight polymer composed of 1000–10,000  $\beta$ -glucose units, the polysaccharide chains are assembled into microfibrils, bundles of microfibrils form cellulose nanofibers that are embedded within a matrix of hemicellulose and lignin [24]. Hemicelluloses are a group of heterogeneous branched polysaccharides whose content in wood typically ranges between 20 % to 30 % by dry weight [24]. Lignins are a family of cross-linked aromatic biopolymers, generally composed of three phenylpropanoids derived from the three monolignols p-coumaryl alcohol, coniferyl alcohol and sinapyl alcohol. Lignin in wood is mainly concentrated in the compound middle lamella and in cell wall corners [25,26], generally more abundant in softwoods (25–30 %), where coniferyl alcohol is the primary building block, than in hardwoods (20–25 %), where sinapyl alcohol is the predominant unit [27,28].

The LIG technique was applied to a wide range of taxonomic softwood and hardwood genera [4,7,29,30], demonstrating promising application in the field of electrocatalysis, capacity pressure sensors and smart home devices [10,30–32].

Currently, only few studies have been carried out on woods commonly called *cedar*. For example, Han et al. [32] investigated red cedar wood (likely referring to the *Juniperus* sp.p. or *Thuja* sp.p.) and Lengger et al. [4] used pristine Indian cedar (*Cedrela toona* Roxb. ex Rottler), an Asiatic hardwood species. The focus of this paper is on *Cedrus* sp. (cedar), a fast-growing cultivation softwood diffused in the Mediterranean area.

The *Cedrus* genus belongs to the *Pinaceae* family and is composed of four species, considered *true cedars*, three of which are of interest from arboriculture and wood-use perspectives [33]: *Cedrus atlantica* (Endl.) Manetti ex Carrière, *C. libani* A. Rich., *C. deodara* (Roxb.) G. Don. These trees have been successfully introduced outside their natural range, primarily in Mediterranean climate zones. For example, in Italy there are more than 3000 hectares of cedar plantations, with 31.3 % being pure cedars and 68.7 % mixed with other species [34]. The wood, durable and resistant to decay, is indistinguishable among the three species. Although these cedars are widespread in several countries for arboriculture, the wood is mostly processed into chips for extractives or biofuel or, limitedly, used for high-quality furniture [35,36].

These peculiarities, combined with the typical features of softwoods in terms of favourable lignin content [23,31,37], make cedar wood an attractive substrate for green LIG technology. To the best of our knowledge, this is the first study focused on the *Cedrus* genus.

In this study, longitudinal sections with sub-radial orientation have been exposed to LIG treatment in ambient condition. Laser power, defocus off-set and laser scribing direction with respect to the wood grain have been systematically changed. The experimental campaign was carried out using pristine and ant flame-treated cedar wood. A comprehensive characterization was performed from the macro- to the nanoscale by optical microscopy (OM), scanning electron microscopy (SEM), X-ray diffraction (XRD),  $\mu$ -Raman spectroscopy and photoelectron spectroscopy (XPS). Thermal profiles were acquired by thermogravimetric analysis (TGA) and electrical properties tested by four-point probe multimeter. On the basis of our best knowledge, in-depth investigation of the effects associated either to the pretreatment of wood with the ant flame or to laser writing direction has not been previously reported.

## 2. Materials and methods

### 2.1. Preparation of neat and pretreated wood

Longitudinal sections of cedar were obtained using a chop saw (*OMS FC 350 RAP*). For this study, sub-radially oriented wood specimens were selected as green LIG substrates. The size of substrates varied between 20 mm x 20 mm and 60 x 60 mm, the thickness was 1 mm or 3 mm.

Dry density and moisture content of cedar wood have been determined on at least four samples following a procedure adapted to the reference standard “EN 13183-1:2002 Moisture content of a piece of sawn timber - Part 1: Determination by oven dry method” and ISO 13061-2:2017 (Physical and mechanical properties of wood -Test methods for small clear wood specimens - Part 1: Determination of moisture content for physical and mechanical tests). Wood substrates were stored in room conditions (approximately 65 % relative humidity (RH) and 20 °C).

The water-based ant flame (*Antiflame, BBT Brandschutz, Switzerland*) was applied twice on both sides of the wood substrates, previously oven dried at 105 °C for 2 h [30,37,38]. In the following, these substrates will be shortly designed as *pretreated wood*. The pretreated wood substrates were stored in a desiccator until further use.

## 2.2. Laser induced graphitization

The single-run laser scribing of pristine and pretreated wood substrates was conducted in room condition using a conventional CO<sub>2</sub> pulsed laser (*Laser TROTEC*, wavelength 10.6  $\mu\text{m}$ , max power 40 W, max scan rate 1800 mm/s) in the following conditions: 1000 DPI (Dots Per Inch), laser power 4–10 %, scan rate 1.75 %, defocus off-set between 0 mm and –5 mm.

It is worth mentioning that the laser source employed for this study is a random polarization beam, meaning that any polarization-dependent effects on the graphitization process are inherently averaged (iRadion Laser. (2023). *Eternity datasheet* (Version 2024-12-16). [https://iradionlaser.com/wpcontent/uploads/2023/06/Ansicht\\_IR\\_Datasheet\\_Eternity\\_20241216.pdf](https://iradionlaser.com/wpcontent/uploads/2023/06/Ansicht_IR_Datasheet_Eternity_20241216.pdf)).

In the following, the green LIG products derived from neat and pretreated substrates will be designed as *N-samples* and *T-samples*, respectively. The lasering direction was systematically varied with respect to the wood grain, *i.e.* orthogonal ( $\perp$ ) or in parallel ( $\parallel$ ). To contain environmental contamination and control the effect of the moisture content, green LIG samples have been stored in a desiccator until further use.

Based on visual inspection, it resulted that the conversion of cedar wood into a continuous carbonaceous layer (namely, *activation*) is optimized for 8 % laser power (max 40 W) and defocusing minimum 3 mm below the focal plane, the scan rate being fixed at 36 mm/s (1.75 % max) (see examples in Fig. 1) [6,29–31].

The designation of the obtained green LIG products is reported in Table 1.

## 2.3. Characterization techniques

- **Optical Microscopy (OM):** the surface morphology was observed adopting an optical stereo microscope (*S9D, Leica, Wetzlar, Germany*) at different magnifications. Photos have been taken using a 12MP camera (*Flexacam C1, Leica, Wetzlar, Germany*) mounted on the microscope.
- **Scanning Electron Microscopy (SEM):** The microstructure was analysed using a field emission scanning electron microscope (FE-SEM

**Table 1**

Sample designation: N, derived from neat cedar wood; T, derived from ant flame-treated cedar wood; O, lased orthogonally to the wood grain ( $\perp$ ); P, lased in parallel to the wood grain ( $\parallel$ )

\* partially activated, x not activated.

Designation	Antiflame treatment	Defocus off-set (mm)	Power (% max)	Laser scribing direction to wood grain	Substrate activation
N3-O	–	–3	8 %	orthogonal	yes
N4-O	–	–4	8 %	orthogonal	yes
N5-O	–	–5	8 %	orthogonal	yes
N3-P	–	–3	8 %	parallel	yes
N4-P	–	–4	8 %	parallel	yes
N5-P	–	–5	8 %	parallel	yes
N5-O (4)	–	–5	4 %	orthogonal	x
N5-O (6)	–	–5	6 %	orthogonal	*
N5-O (10)	–	–5	10 %	orthogonal	*
N5-P (4)	–	–5	4 %	parallel	x
N5-P (6)	–	–5	6 %	parallel	*
N5-P (10)	–	–5	10 %	parallel	*
T0-O	yes	0	8 %	orthogonal	x
T1-O	yes	–1	8 %	orthogonal	x
T2-O	yes	–2	8 %	orthogonal	yes
T3-O	yes	–3	8 %	orthogonal	yes
T4-O	yes	–4	8 %	orthogonal	yes
T5-O	yes	–5	8 %	orthogonal	yes
T3-P	yes	–3	8 %	parallel	yes
T4-P	yes	–4	8 %	parallel	yes
T5-P	yes	–5	8 %	parallel	yes

*Leo-SUPRA™ 35, Carl Zeiss SMT, Oberkochen, Germany*) operating at a low-range accelerating voltage (1.5, 2, 5 and 10 kV).

- **Thermogravimetry (TGA):** analyses were performed with a *TG-DSC (STAR system 1, Mettler Toledo, Columbus, United States)* in nitrogen flow 100 mL/min on 10 mg of powdered wood sample placed in an open alumina crucible. The following thermal treatment was then performed: isothermal step at 115 °C for 10 min to remove hygroscopic water, followed by 20 °C/min ramp from room temperature to 900 °C.

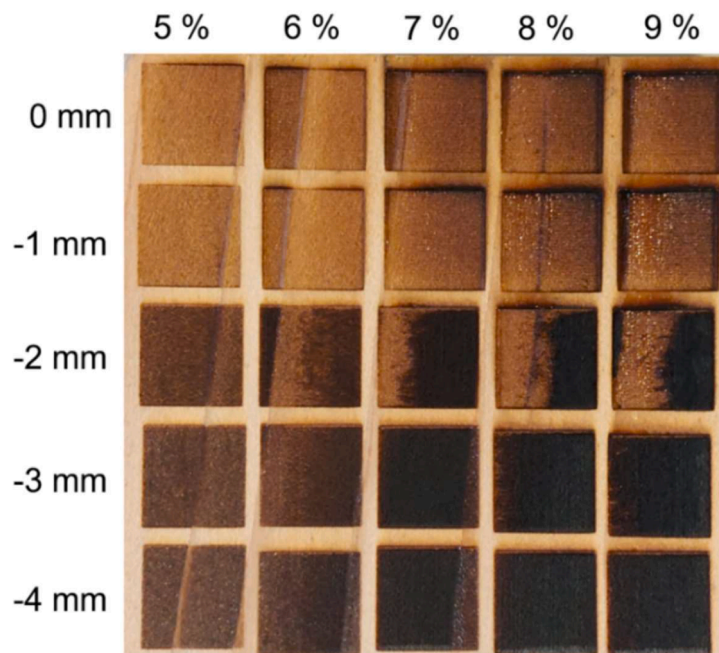


**Fig. 1.** Photos of green LIG products derived from cedar wood: defocus off-set (vertical rows), laser power (horizontal rows, percentage of the maximum value 40 W), scan rate 36 mm/s.

- **X-ray diffraction analysis (XRD):** diffraction patterns were collected using a diffractometer (*X-Pert Pro, Philips, Amsterdam, Netherlands*), in the following conditions: Cu K $\alpha$  radiation  $\lambda = 0.15418$  nm,  $2\theta$  range  $10^\circ - 60^\circ$ , step size  $0.02^\circ$  and scan rate  $0.6^\circ/\text{min}$ . Moreover, diffraction patterns were acquired on powdered green LIG samples using a *Smart Lab SE* diffractometer (*Rigaku, Japan*) in the following conditions: Cu K $\alpha$  radiation  $\lambda = 0.15418$  nm,  $2\theta$  range  $5^\circ - 80^\circ$ , step size  $0.01$  and scan rate  $0.5^\circ/\text{min}$ .
- **X-ray photoelectron spectroscopy (XPS):** X-ray photoemission and photo-induced Auger spectra were collected using an *ESCALAB MkII (VG Scientific, Ltd. - East Grinstead, UK)* spectrometer, equipped with a standard Al K $\alpha$  excitation source and a 5-channeltron detection system. The spectra were collected at 40 eV constant pass energy. XPS measurements were carried out approximately at the centre of the samples, the analysed area was about  $1\text{ cm} \times 1\text{ cm}$ . The binding energy (BE) scale was calibrated by positioning the peaks of Au 4f $_{7/2}$  from the reference sample, and C 1s peak from adventitious carbon, at BE=84.0 and 285.0 eV, respectively. The accuracy of the measured BE was  $\pm 0.1$  eV. Spectroscopic data were collected and processed by the *Avantage v.5.9* software (*Thermo Fisher Scientific, Ltd. - East Grinstead, UK*), using a peak-fitting routine with symmetrical Gaussian-Lorentzian functions. The Shirley background was subtracted from the photoelectron spectra.
- **Raman spectroscopy:**  $\mu$ -Raman analysis was performed at room temperature using a *Renishaw RM2000 (Renishaw, Gloucestershire, UK)* equipped with a Peltier-cooled charge-coupled device (CCD) camera, in conjunction with a *Leica* optical microscope. Measurements were performed using the  $\times 50$  objective (laser spot diameter of about  $1\ \mu\text{m}$ , excitation line 785 nm). The analysis was performed in the centre of the rectangular LIG trace of size  $2 \times 1\text{ cm}^2$ . For selected samples, measurements were also acquired along the two edges. The spectra were then processed by *Fityk0.9.8* software, subtracting a linear background, to take in account the natural luminescence of wood.
- **Electrical characterization** of rectangular LIG traces ( $5 \times 1\text{ cm}^2$ ) was performed through the four-point probe (FPP) method [30,32,39]. The probe was always positioned along the lasing direction. The FPP relies on a 4-wire resistance measurement in the centre of the sample ( $\Delta V/\Delta I$ ) to compute the sheet resistance  $R_s$  under the assumption of thin film (*i.e.* the thickness of the trace is lower than 40 % the spacing between the probes [39]).

$$R_s = \frac{\pi}{\ln(2)} \frac{\Delta V}{\Delta I} C_f \quad (1)$$

A correction factor  $C_f$  is generally needed to account for the finite size of the sample. This coefficient, indeed, considers the reflection of the injected current at the edge of the sample and, thus, is related to its geometry [39,40]. In our setup, the sheet resistance was evaluated by means of the four-point probe station *Ossila* (<https://www.ossila.com/products/four-point-probe-system>), the probes' spacing was equal to 1.27 mm. Based on the described configuration, a correction factor  $C_f$  close to unity (0.9) was chosen. To assess measurement reliability, sheet resistance was recorded three times, the average values and corresponding standard deviations are reported in Table 3.

### 3. Results and discussion

#### 3.1. Density, microstructure and pyrolysis of neat and pretreated wood

The calculated dry density was  $0.47 \pm 0.03\text{ g/cm}^3$ . In this respect, Lengger et al. [4] recently recommended to employ high-density ( $> 0.5\text{ g/cm}^3$ ) hardwoods, in order to minimize inhomogeneities that might adversely affect the electrical properties of the resulting green LIG

layers. The moisture content was  $12.1 \pm 0.9\%$  [41], as expected for equilibrium moisture content (EMC) of wood in room conditions [42], evidencing that the timber used is a *seasoned wood*. This is a key-point, since LIG technology is not effective on green wood [31].

On the cross section, the mesostructure of cedar is characterized by a pattern of longitudinally oriented tracheids, with cell walls that progressively thicken from earlywood to latewood in the growth rings. The lumina of the tracheids measured approximately few tens of  $\mu\text{m}$  (Fig. 2a).

The majority of cells in wood are oriented along the longitudinal direction, typical cell length to width ratio of softwood tracheids ranges from 70:1 to 100:1 [41]. The sub-radial longitudinal section is marked by uniseriate parenchymal rays, composed by single rows of cells; the tracheids are scattered by the presence of bordered pits, typical of softwood timbers (Fig. 2b-d).

In this study sub-radial longitudinal sections have been selected aimed to minimize local microscopic heterogeneities [ref]. The alternating growth layers within the annual rings create a characteristic pattern of light and dark strips, clearly visible to the naked eye, that provide a reliable means of identifying the longitudinal direction within the anisotropic nature of the wood specimen (see Graphical Abstract). It is worth mentioning that transverse sections were excluded due to the presence of extended macroporosity associated to the ensemble of aligned hollow anatomical elements (Fig. 2a) [4].

In order to investigate the actual effect of the antifiame on cedar wood, XRD and TGA were performed (Figs. 3 and 4) [37]. The XRD patterns of the antifiame revealed that the employed product is based mainly on ammonium phosphates, as expected according to the information provided by the producer, and possibly on a silicon phosphate phase [43] (Fig. 3 upper panel). The pattern of the pretreated wood shows the characteristic reflections of crystalline cellulose [44] combined with several extra peaks. In details, the four peaks in the  $2\theta$  range  $15^\circ - 18^\circ$  and the peak around  $2\theta = 26.3^\circ$  can be attributed to the antifiame whereas the labelled (+) extra-peaks at  $2\theta = 21.4^\circ$ ,  $23.5^\circ$  and those within  $27.2^\circ - 29.4^\circ$  evidence the presence of additional crystalline phases (in the following called *flame-retardancy phases*) (Fig. 3 lower panel).

Thermogravimetry evidenced that the pyrolysis of the pristine wood (Fig. 4, black curve) occurs within  $200^\circ\text{C}$  and  $400^\circ\text{C}$  accompanied by a weight loss of about 80 %, mainly due to the thermal decomposition of hemicelluloses and cellulose [45–48], leaving at  $900^\circ\text{C}$  approximately 20 % by weight of residue (*biochar*). Instead, the thermal degradation profile of the pretreated wood (Fig. 4, red curve) develops through endothermic events approximately within  $200 - 300^\circ\text{C}$  associated to about 30 % weight loss followed by further 60 % weight loss in the range  $400 - 800^\circ\text{C}$  that occurred exothermically in two distinct steps, finally leading to a 10 % by weight of residue at  $900^\circ\text{C}$ . According to the results in Fig. 4, the lower-temperature weight-loss has to be associated to the pyrolysis of the *flame-retardant phases*, possibly combined with the thermal decomposition of unreacted ammonium phosphates. In fact, diammonium hydrogen phosphate decomposes at  $87^\circ\text{C}$  in ammonia and ammonium dihydrogen phosphate which further leads within  $145 - 167^\circ\text{C}$  to phosphoric acid and ammonia, finally giving rise in the range  $220 - 540^\circ\text{C}$  to phosphoric anhydride and water (Fig. 4, blue curve) [49–51]. Reasonably, based on the thermal profile on the antifiame (Fig. 4, blue curve), the following weight losses occurring within  $550 - 750^\circ\text{C}$  refer to the subsequent transformations of by-products derived from the thermal decomposition of the antifiame, including the sublimation of phosphoric anhydride [51].

Concluding, the combination of XRD and TG results demonstrate that the flame-retardancy of cedar wood occurred through the interaction at room temperature between wood and the antifiame resulting in newly-formed crystalline phases (*flame-retardancy phases*), giving rise to a material (*pretreated wood*) characterized by decreased resistance to pyrolysis (compared to pristine wood). According to Grexa et al. [49], the flame-retardancy action is based on the esterification between cellulose

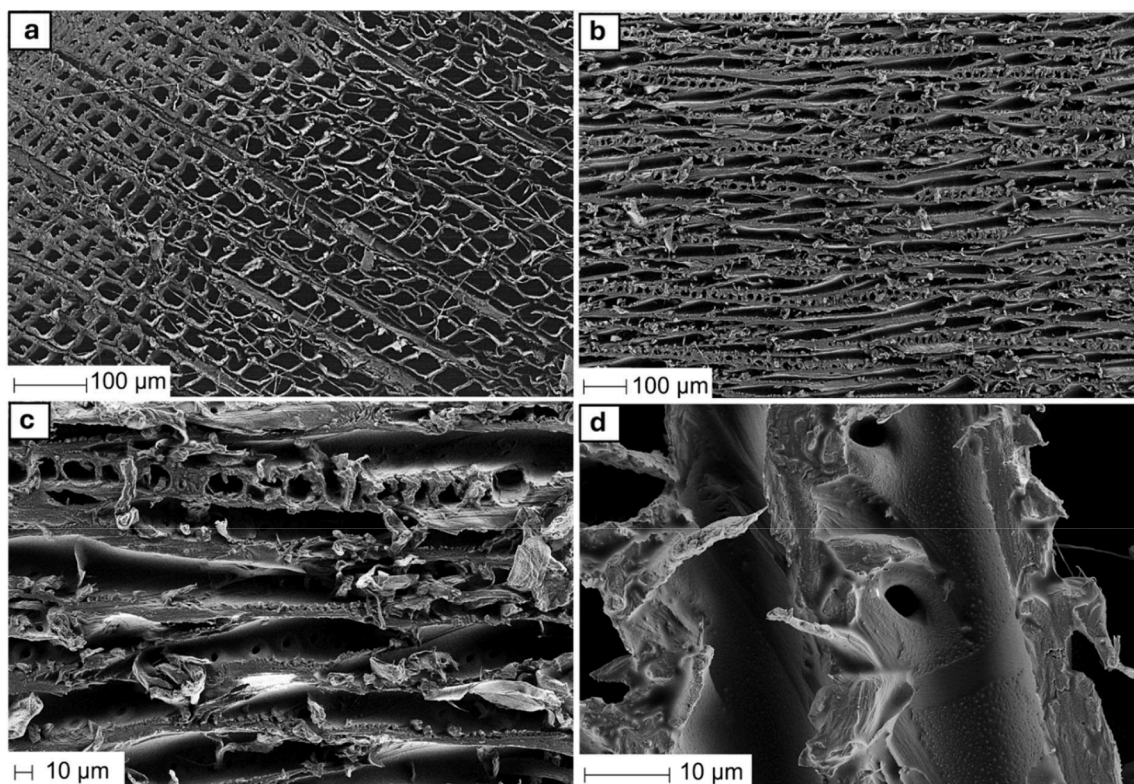


Fig. 2. Scanning Electron Microscopy (FE-SEM) micrographs of cedar wood (a) transversal-cut (cross-section) (b-d) longitudinal cut (sub-radial section).

and phosphoric acid, water is released, dehydration of wood is promoted, the combustion rate decreases due to the reduced oxygen permeability, finally leading to an increased amount of *biochar* (compared to pristine wood) (Fig. 4).

### 3.2. Microscopy

The morphological and microstructural features of green LIG samples obtained using different process parameters have been investigated. As an example, samples N5-O and T5-O are compared in Fig. 5. Sample N5-O shows a homogeneous crack-free 3D microstructure characterized by diffused porosity due to the photothermal decomposition of cellulose, hemicellulose and lignin accompanied by the release of gaseous by-products [31,32,38]. Interestingly, N5-O showed on the macro-scale a sharp distinction in correspondence of contiguous growth rings (Fig. 5a). Instead, T5-O was characterized by a denser microstructure and deep longitudinal macro-defects (width about 100 μm) (Fig. 5b and 5d) (paragraph 3.6). Moreover, Fig 5a-b evidenced that the step between the bare wood and the LIG traces was nearly undetectable at the macro-scale, to indicate that the selected process parameters allowed to minimize the ablation process [31]. Considering also the thickness of the layers derived from neat wood (e.g. 150 μm, Fig. 5e), it can also be assessed that these green LIG products were formed within the *optimized heat-accumulation region* (as expected for the fixed writing speed of 36 mm/s) [6]. In fact, the synthesis of green LIG products proceeds via a photo-thermal route, a process dominated by thermal effects through heat accumulation combined with photo-assisted phenomena, that, through a complex thermochemical mechanism, induces the onset of *carbonization* and *graphitization* of the bio-based source [6,31]. Finally, in Fig. 6a-d are compared the high-magnification FE-SEM micrographs of N3-O and N5-O. The two samples, laser-scribed along the  $\perp$  direction at different defocusing, consisted of dense meshes that delimited a network of voids, pores and cavities whose size range, approximately, from few to hundreds μm (Figs. 6a-b and 7a-b). Samples N3-O and N5-O showed analogous microstructural features, even if N5-O seemed more

regularly and oriented (Fig. 6c-d).

For the sake of comparison, the high-magnification FE-SEM micrographs of T3-O and T5-O are shown in Fig. 6e-f and 6g-h. Clearly, these LIG traces derived from ant flame-treated substrates in the same experimental conditions of N3-O and N5-O led to products characterized by additional diffused micro-porosity, especially in the body of network meshes (Fig. 7c-d). The effect, particularly evident in sample T5-O, has to be associated to the release of gaseous by-products related to the thermal decomposition of unreacted ant flame and flame-retardancy phases (paragraph 3.1) [32].

### 3.3. X-ray photoelectron spectroscopy (XPS)

The surface chemical composition of the samples was investigated by XPS. As expected, all samples are characterized by the dominant presence of carbon, namely 74.6 at % for neat wood, 75.6 at % for N5-O and 70.9 at % for T3-O. Fig. 8 shows the comparison of C 1s signals deconvoluted by a peak-fitting routine, introducing three synthetic peaks, located at BE = 285.0 eV, 286.7 eV and 288.7 eV, assigned to C-C (Fig. 8 C1s-1), C-O and C=O (Fig. 8 C1s-2), -COOH(R) (Fig. 8 C1s-3), respectively. The area ratio of C1s-1/C1s gives the relative abundance of C-C bond, the obtained value is 54 % for neat wood, increasing to 66 % and 67 % for sample N5-O and T3-O, respectively (Fig. 8).

In order to quantify the abundance of carbon atoms hybridized  $sp^2$  and  $sp^3$ , the well-established method of *D* parameter was employed [52]. The *D* parameter value for pristine wood was 13.8 eV, indicating that most of carbon atoms are hybridized  $sp^3$  (97.0 %). For green LIG samples the value of *D* parameter was 14.8 eV for N5-O, consisting of 15 % C of carbon hybridized  $sp^2$  and 85 % of carbon hybridized  $sp^3$ , and 16.0 eV for T3-O, revealing the presence of 31.2 % of carbon hybridized  $sp^2$  and 68.8 % of carbon hybridized  $sp^3$  (Fig. 9). XPS analysis showed also the presence of oxygen, phosphorous and nitrogen, besides traces of surface contaminants (i.e. Ca, Fe and Si). The calculated C/O atomic ratio of neat wood was 2.9, whereas the values for N5-O and T3-O were 3.4 and 3.5, respectively. Small amounts of phosphorous (3.8 at %) and

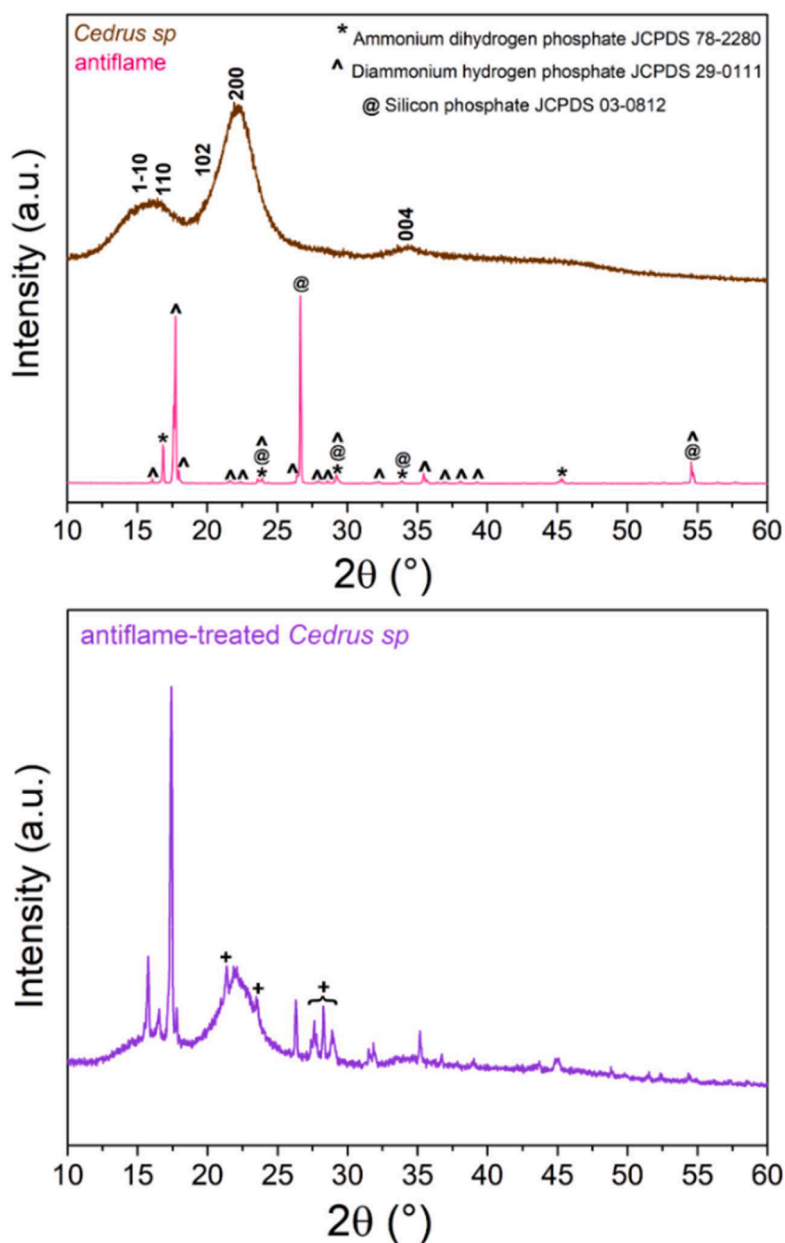


Fig. 3. X-ray diffraction (XRD) spectra of pristine wood and antiflame (upper panel), antiflame-treated wood (lower panel).

nitrogen (1.9 at %) were detected in sample T3-O, mostly phosphates and amines, residuals of the antiflame. The results of XPS analysis were in line to what it was expected for green LIG products derived from lignocellulosic substrates. In fact, during laser irradiation the removal of oxygen functional groups occurs simultaneously with the conversion of carbons from  $sp^3$  to  $sp^2$ . The efficiency of these photochemical events depends directly on the operation parameters deputed to control the level of exposure of the substrate to the laser source [6]. Moreover, as expected, XPS analysis outlined that the antiflame, due to reduced oxygen permeability, favoured the *graphitization* process [6,49,53] (*paragraph 3.6*).

### 3.4. $\mu$ -Raman spectroscopy

Raman spectroscopy is a well-recognized technique for the structural characterization of carbon-based materials, such as graphite, diamond, graphene, carbon nanotubes, fullerene, and amorphous carbon [54]. The most prominent features in the Raman spectra of graphitic materials

are the so-called G band around  $1580\text{ cm}^{-1}$ , the 2D band around  $2700\text{ cm}^{-1}$  and the D band around  $1350\text{ cm}^{-1}$ . The G band is due to the doubly degenerate  $E_{2g}$  symmetry phonon mode at the Brillouin zone centre, corresponding to the in-plane stretching motion between  $sp^2$  carbon atoms. The 2D band originates from a second-order resonance process involving inter-valley scattering assisted by optical phonons and defects [55,56]. The D band results from the  $A_{1g}$  symmetry breathing modes of  $sp^2$  rings and appears in the presence of defects, such as edge effects and dangling  $sp^2$  carbon bonds [57]. Change in shape, position and relative intensity, especially of G and 2D Raman bands, could be indicative of inner structure of the carbon-based material, the presence of defects and, for graphite-based materials, the number of layers. In carbon-based materials, the ratio of the D band intensity to the G band intensity ( $I_D/I_G$ ) is also widely used to estimate the crystallinity degree and, consequently, the level of disorder. The  $I_D/I_G$  ratio of poorly-ordered carbonaceous material typically lies within 1 to 2.6 whereas highly-crystalline graphite is characterized by significant lower  $I_D/I_G$  values that range within 0.01 and 0.3 [58,59]. The  $I_D/I_G$  ratio tends to increase with

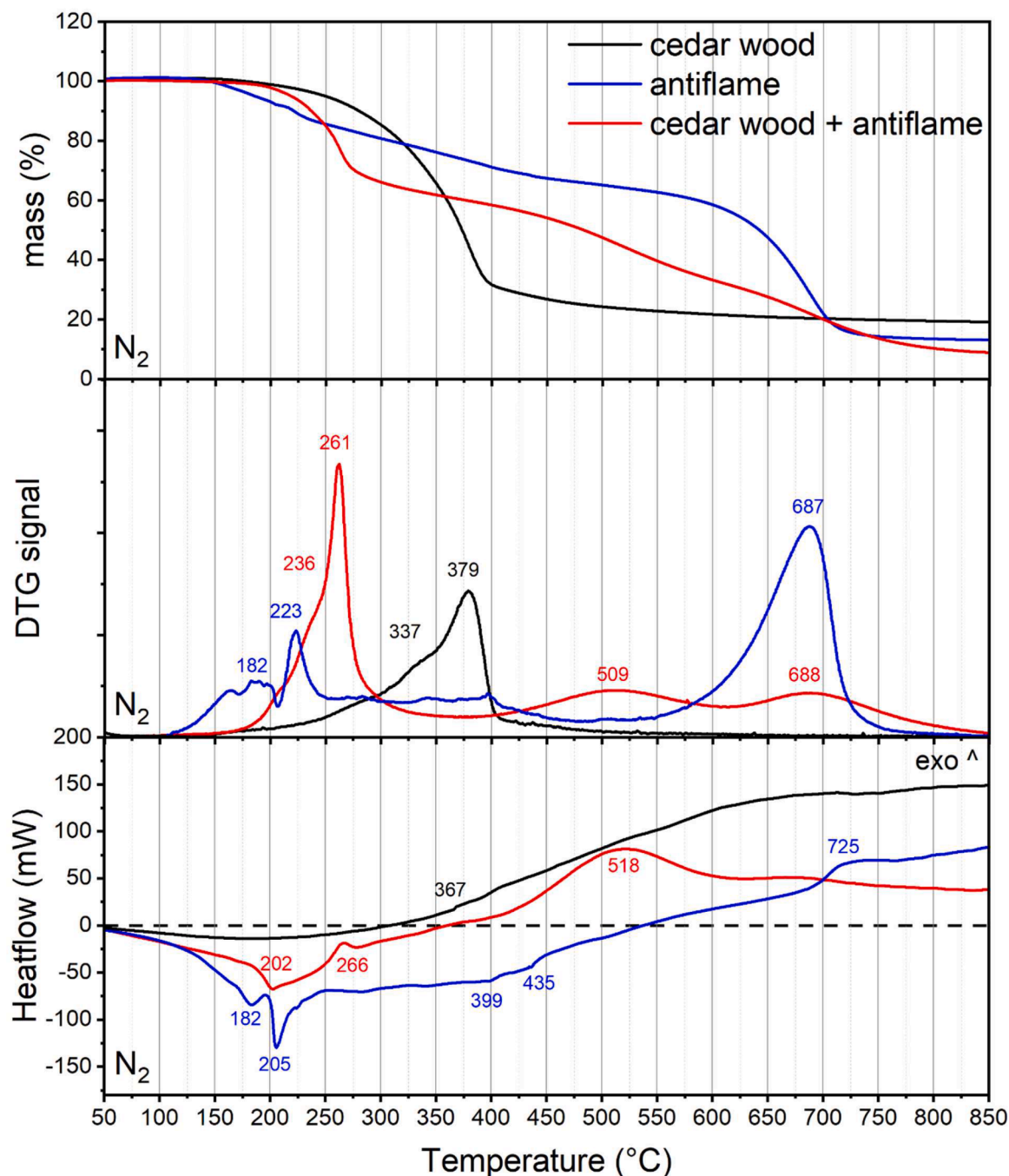


Fig. 4. Thermogravimetry (TG), first derivative of thermogravimetry (DTG) and heat flow of: neat wood (black line), ant flame-treated wood (red line) and ant flame (blue line).

decreasing size of graphite, due to the presence of edge defects, and increasing the oxidation degree. Furthermore, taking in account the dependence from Raman laser wavelength, the following correlation between  $L_a$  (nm) and the band intensity ratio  $I_D/I_G$  has been developed [60,61]:

$$L_a(\text{nm}) = 2.4 \cdot 10^{-10} \cdot \lambda^4 / (I_D / I_G) \quad (2)$$

where  $\lambda$  is the wavelength (in nm) of the laser source used for the Raman characterization.

A full set of data was obtained from the analysis of the acquired Raman spectra (Table 2).

The position and the shape of D band and G band and the calculated  $I_D/I_G$  ratios (1.25–2.79) evidenced that the obtained LIG traces are

prevalently constituted by amorphous carbons associated to high-defective graphitic domains [4,53,62–64]. Indeed, some spectra showed also the 2D peak around  $2700 \text{ cm}^{-1}$  (Fig. 10a-b) [4], suggesting the presence of graphene-like nanostructures, frequently named *multi-layer graphene* [29,31,65]. It is worth mentioning that the small laser spot used to acquire the Raman spectra in the middle of the LIG traces did not always allowed to clearly ascertain the presence of the 2D band (Fig. 12).

According to the data reported in Table 2, it resulted that the  $I_D/I_G$  ratio, and consequently the  $L_a$  values, of  $\perp$ -scribed samples derived from pristine wood (N3-O, N4-O, N5-O) varied within a narrow range. Instead,  $\parallel$ -scribed traces (N3-P, N4-P, N5-P) were more sensitive to the defocus off-set and a decreasing trend of the  $I_D/I_G$  ratios, associated to a

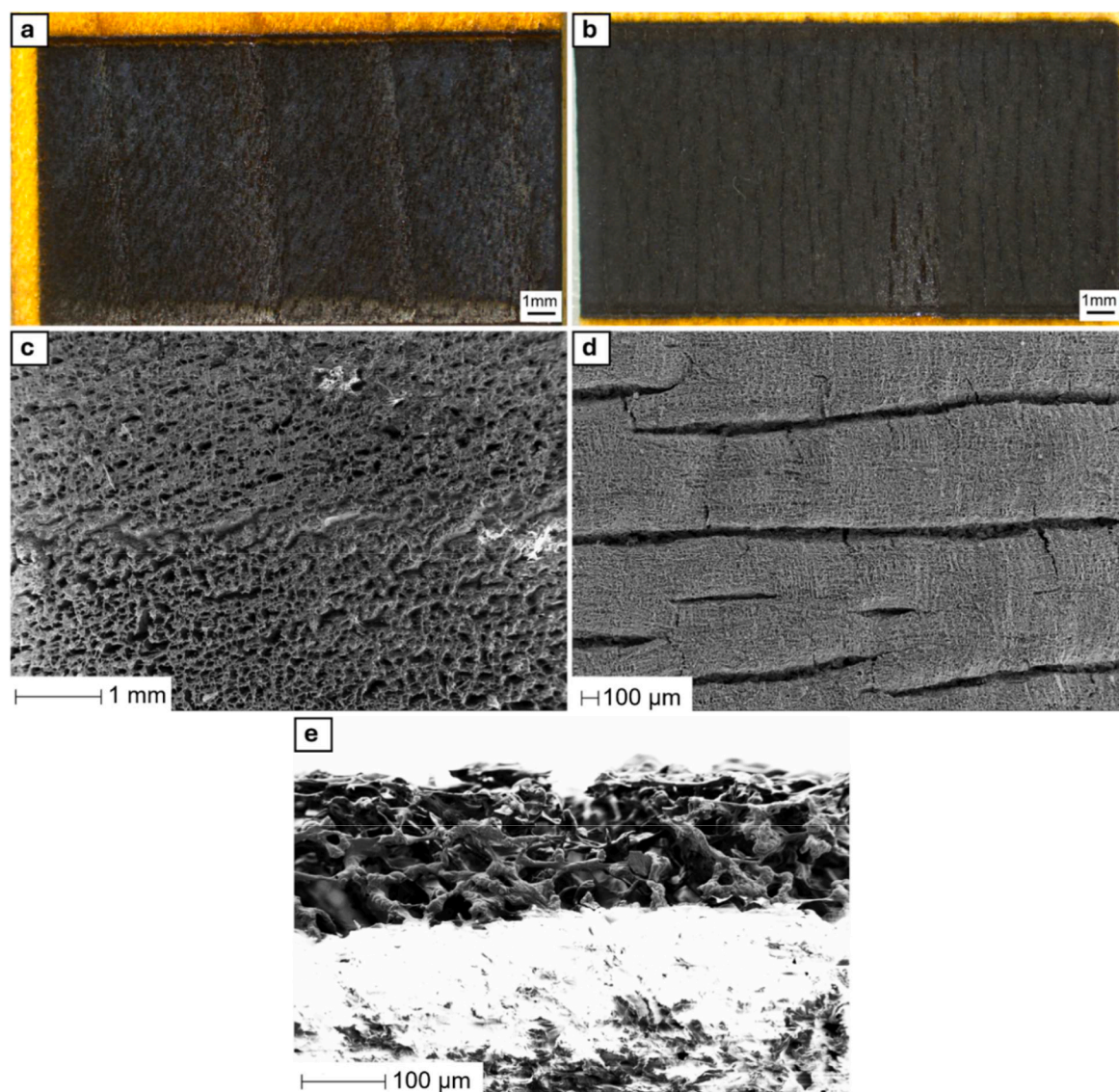


Fig. 5. Optical Microscopy (OM) photographs and Scanning Electron Microscopy (FE-SEM) micrographs of (a-c) N5-O (top view), (b-d) T5-O (top view), (e) N5-O (side view).

progressive increase of the in-plane crystallite size  $L_a$ , was observed (Fig. 11 and Suppl. Fig. S1).

These results put into evidence the trend of graphitic domains' defectiveness as a function of defocusing off-set and lasing direction (paragraph 3.6). In this respect, it can be interestingly observed that fixing the defocusing at  $-4$  mm or  $-5$  mm, the  $I_D/I_G$  ratios of  $\perp$ -scribed samples (cellulose-rich direction) are higher compared to those of  $//$ -scribed ones (lignin-rich direction) (Suppl. Fig. S1). It has been established that polysaccharides, including cellulose and hemicelluloses, generally require a stronger laser exposure to achieve graphitization degrees comparable to those reached by aromatic-rich substrates and are converted in carbonaceous materials characterized by higher defectiveness than aromatic-based polymers (e.g. lignin) [6, 29,32,37,38]. Thus, given the well-known wood ultrastructure [22–28], it can be reasonably supposed that sample N3-P (lignin-rich-direction) reaches a higher degree of graphitization with respect to N3-O (cellulose-rich direction) (paragraph 3.6)

Finally, Raman spectroscopy evidenced that the pretreatment of cedar wood with the ant flame had a minimal positive effect on samples laser-scribed  $\perp$  to the wood grain (Table 2). In fact, samples T3-O, T4-O and T5-O showed only a slight reduction of the  $I_D/I_G$  ratios when

compared to those of the respective samples derived from neat wood (e.g. N3-O, N4-O and N5-O).

Finally, to investigate the homogeneity of the obtained green LIG traces, a series of  $\mu$ -Raman spectra was also acquired along the edges of the engraved surface. As an example, in Fig. 12 the spectra recorded for sample N5-O are reported. The spotted areas showed similar features in terms of peak position, intensity and width to evidence that an overall ultra-structural uniformity has been achieved.

### 3.5. X-ray diffraction

In Fig. 13 the spectra of representative LIG samples derived from neat cedar wood are compared.

All XRD patterns showed the characteristic peaks of crystalline cellulose [44]. Additionally, the spectrum of sample T3-O showed the labelled (+) extra-peaks at  $2\theta = 23.5^\circ$  and  $28.9^\circ$  (Fig. 3) and reflections in the  $2\theta$  range  $15^\circ - 18^\circ$  and at  $2\theta 26.1^\circ$  attributed to residue of thermal decomposition of unreacted ant flame and flame-retardancy phases (paragraph 3.1).

In order to get evidence of the graphitic phases, selected XRD spectra were also collected on green LIG samples in powder form (Fig. 14). All

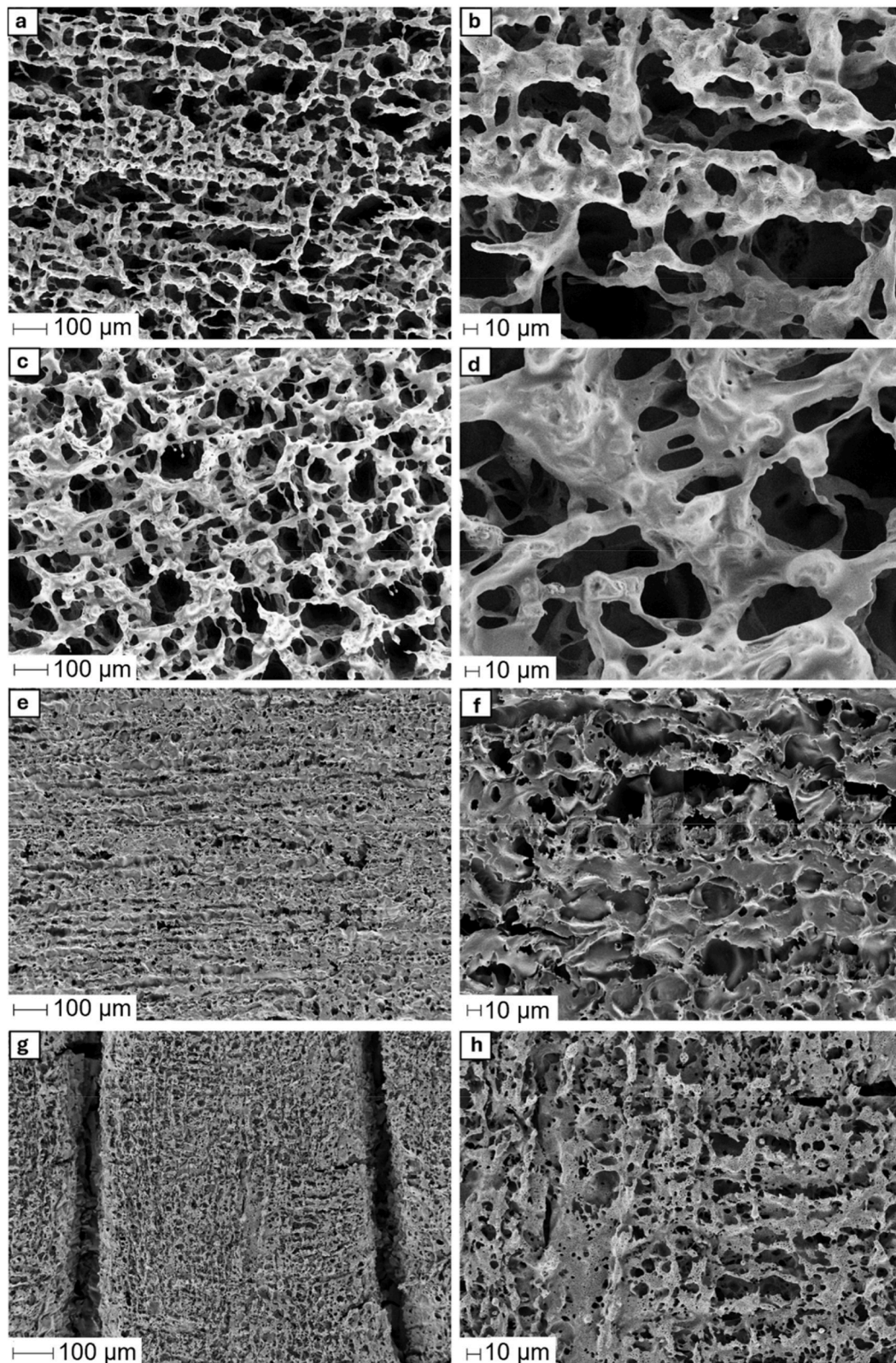


Fig. 6. Scanning Electron Microscopy (FE-SEM) micrographs (top view) of (a-b) N3-O, (c-d) N5-O, (e-f) T3-O and (g-h) T5-O.

the spectra evidenced the presence of a broad peak at  $2\theta$  about  $22.4^\circ$  and a small signal at  $2\theta$  about  $15^\circ$ , both reflections are attributable to crystalline cellulose [44]. Distinctly, the XRD pattern of sample N3-O revealed also a shoulder at  $2\theta$  about  $26^\circ$  and a small broad peak at  $2\theta$  around  $43.4^\circ$  that might be ascribed to the (002) e (100) reflections of

graphite, despite the shift respect to the fully crystalline material [10, 66]. Actually, the feature at  $43.4^\circ$  could also be evidenced in the spectra of N5-P and N5-O samples. N3-P presents a very similar XRD profile, but the low amount of sample available for the analysis makes more evident the amorphous contribution of the glass slide holder. Thus, in line with

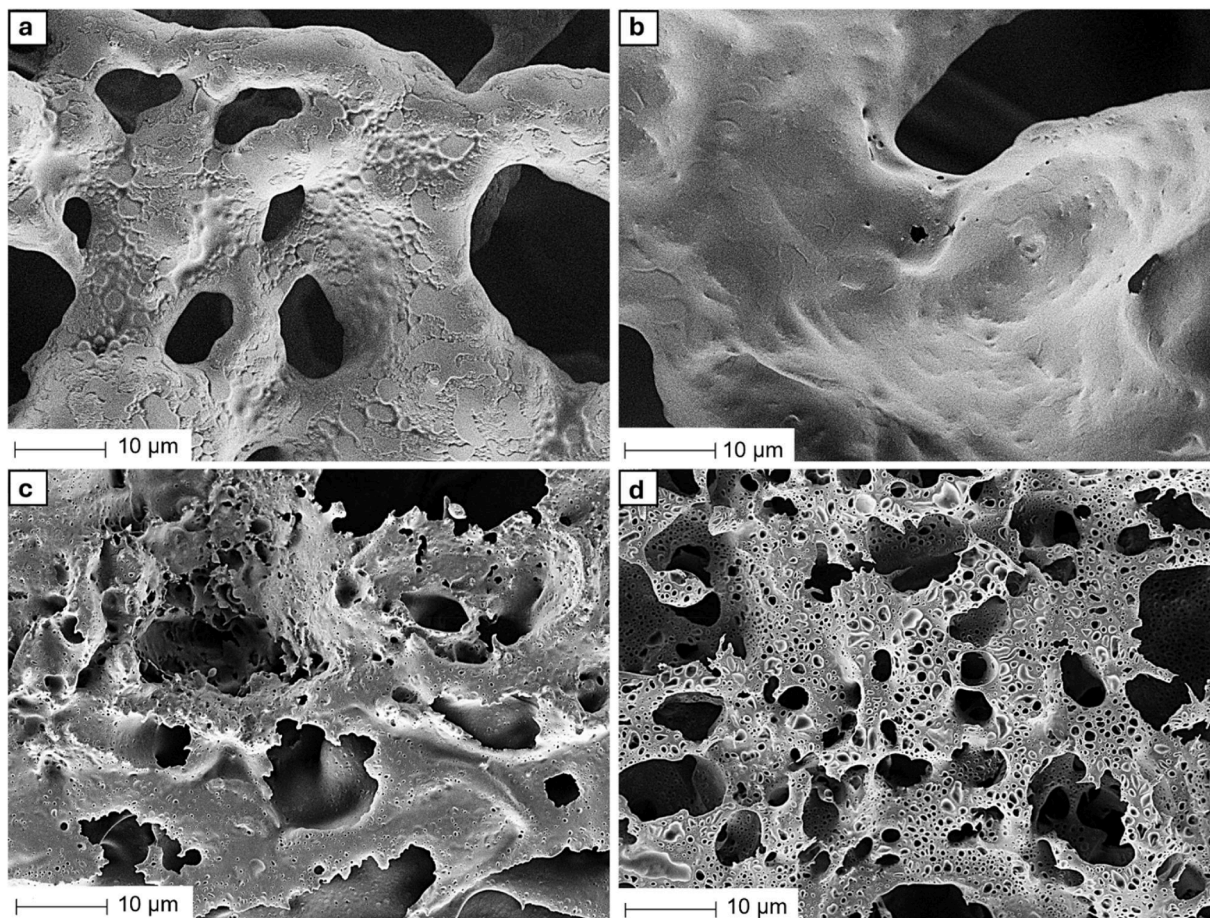


Fig. 7. Scanning Electron Microscopy (FE-SEM) micrographs (top view) of (a) N3-O, (b) N5-O, (c) T3-O and (d) T5-O.

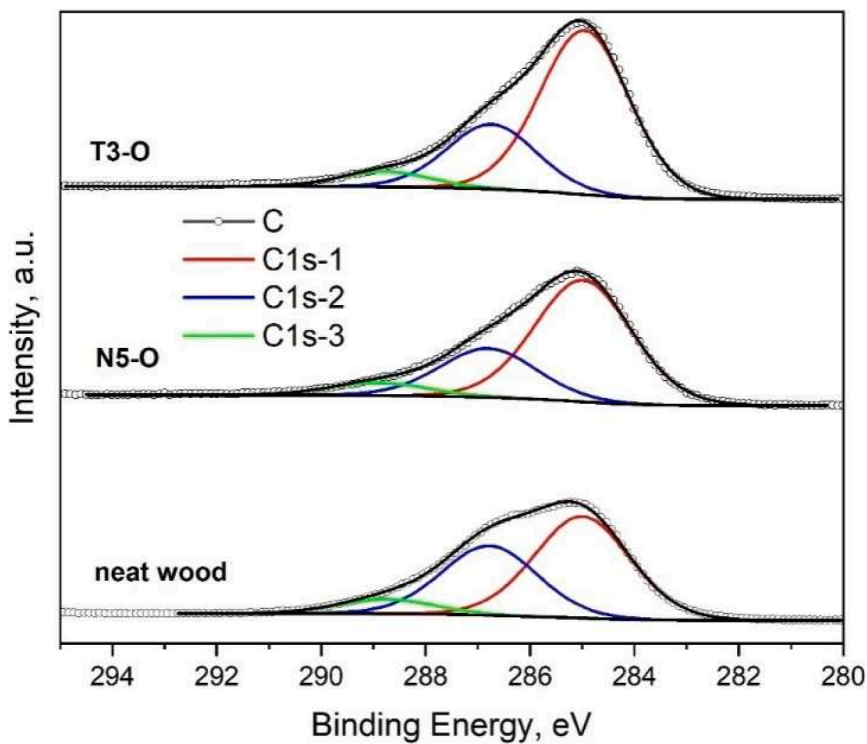


Fig. 8. Comparison of C1s signals of neat wood and selected green LIG samples (N5-O and T3-O): C (C1-s carbon), C1s-1 (C-C, C-H), C1s-2 (C-O, C=O), C1s-3 (-COOH(R)).

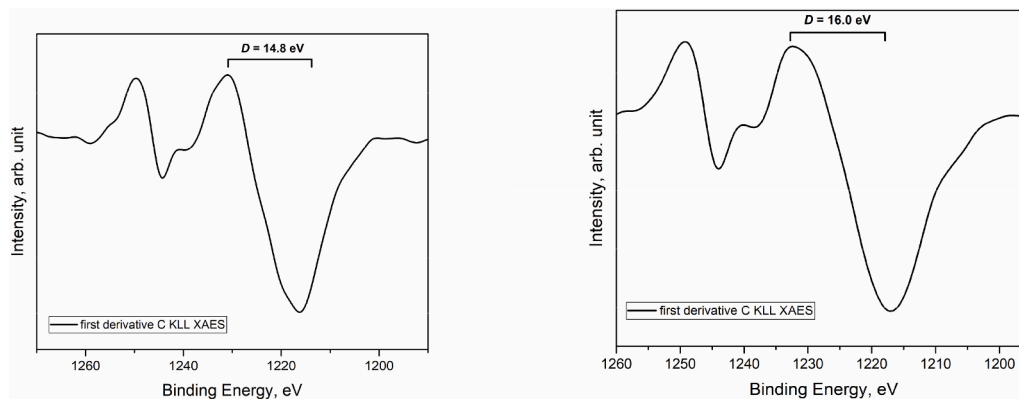


Fig. 9. Calculated D-parameter of green LIG samples N5-O (left panel) and T3-O (right panel).

Table 2

Results of  $\mu$ -Raman spectroscopy acquired in the centre of the LIG traces (due to the high fluorescence background, spectra of T2-O, T3-P and T4-P are not available).

Sample	Position $\text{cm}^{-1}$	Intensity a.u.	Width FWHM $\text{cm}^{-1}$	$I_D/I_G$	$L_a$ Nm
N3-O	D band 1299	5286	128	1.9	48.0
	G band 1581	2708	82		
N4-O	D band 1299	3436	128	2.3	39.6
	G band 1588	1501	75		
N5-O	D band 1300	2281	135	2.1	43.4
	G band 1590	1064	71		
N3-P	D band 1303	2819	292	2.8	32.6
	G band 1570	1009	124		
N4-P	D band 1324	1558	112	1.4	65.1
	G band 1580.2	1094	101		
N5-P	D band 1327	1957	200	1.2	75.9
	G band 1562.6	1563	156		
T3-O	D band 1309.8	13,177	92	1.8	50.6
	G band 1561.7	7239	151		
T4-O	D band 1302.7	14,572	168	2.0	45.6
	G band 1559.9	7268	163		
T5-O	D band 1304.6	21,884	204	2.0	45.6
	G band 1566.5	10,820	121		
T5-P	D band 1332.2	47,391	283	2.4	38.0
	G band 1556.9	19,961	124		

Raman spectroscopy (paragraph 3.4), these results suggest that green LIG traces derived from pristine wood substrates show a prevalently amorphous  $\text{sp}^2$  carbon phase.

### 3.6. Electrical properties

The results of the electrical properties in terms of sheet resistance ( $R_s$ ) are presented in Table 3.

The FPP measurements showed that an optimal off-set has been identified between  $-3$  mm and  $-4$  mm. Indeed, higher off-sets drastically reduced the conductivity of the green LIG products derived from neat and pretreated wood substrates. Defocusing is a highly impacting parameter with a non-monotonic trend regardless of the type of wood and the lasing direction. The laser treatment on the focal plane (off-set 0 mm) leads to the ablation of the sample rather than its conversion into a conductive 3D carbonaceous layer.

The lowest sheet resistance, approximately  $40 \text{ } \Omega/\text{sq}$ , was achieved for N3-P and T3-O. It is worth mentioning that  $50 \text{ ohm}/\text{sq}$  can be considered a threshold for LIG applications [67]. For instance, by comparing the performance of antennas having the same layout but fabricated with standard conductors (e.g. copper, silver, aluminium) and the obtained green LIG traces, the lowest herein measured sheet resistance, i.e.  $37 \text{ } \Omega/\text{sq}$  for T3-O, corresponds to a 60 % decrease of the radiation efficiency compared to metals, and thus approximately a 40 % reduction of the read range. Low values of sheet resistance are also preferable for energy-storage devices, such as supercapacitors, whose ratio between the energy accumulated during the charge phase and the one delivered during the discharge is proportional to the ohmic losses of the conductor [68]. In contrast, a higher sheet resistance could not be detrimental for differential sensors (e.g. gas, temperature, strain, relative humidity), which rely on variations of the resistance, rather than on the nominal value, to transduce stimuli [69,70].

It is to be highlighted that the intrinsic nature of LIG traces might determine unstable electrical measurements [71]. However, it is well known that the FPP method eliminates the contribution of the contact

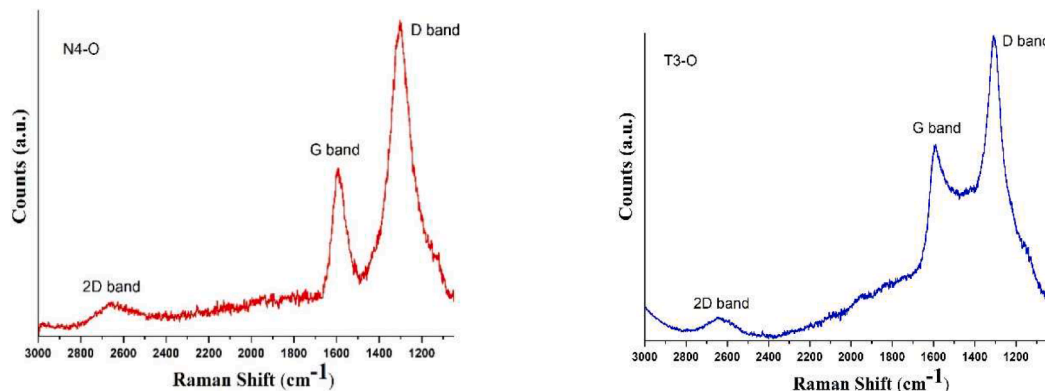


Fig. 10.  $\mu$ -Raman spectra of N4-O (left panel) and T3-O (right panel).

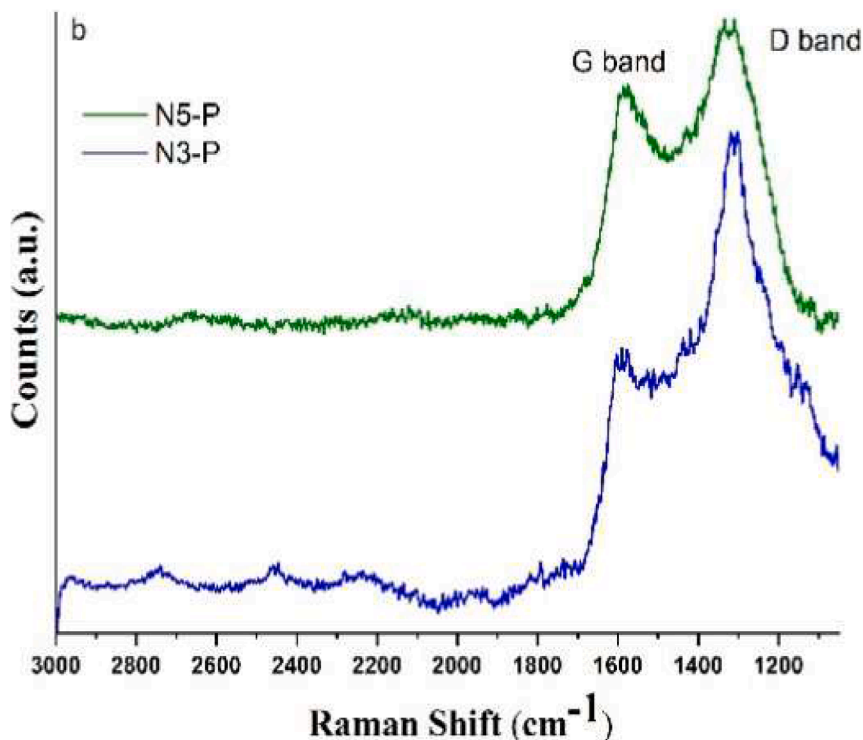


Fig. 11.  $\mu$ -Raman spectra of green LIG samples N3-P and N5-P.

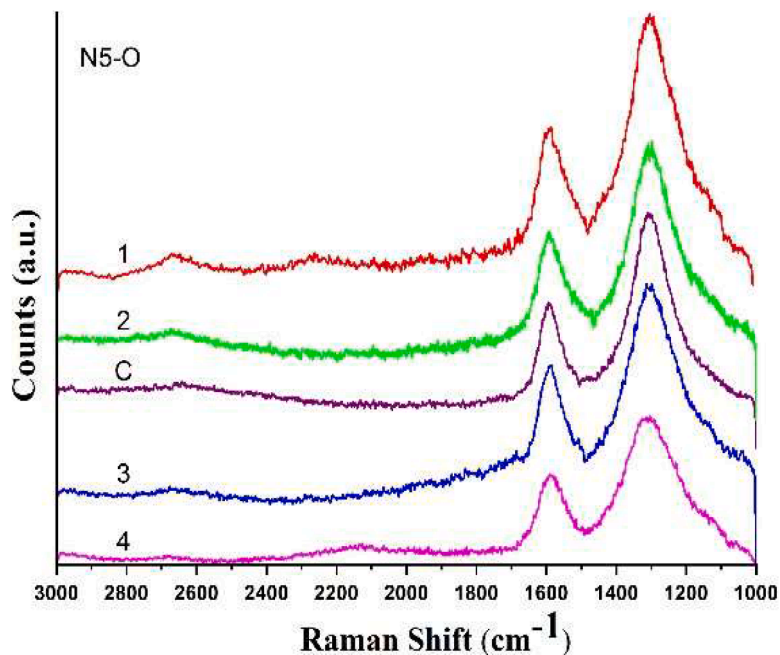


Fig. 12.  $\mu$ -Raman spectra of N5-O acquired in the different points of the rectangular ( $2 \times 1 \text{ cm}^2$ ) LIG trace: C (central), 1 and 2 (top corners), 3 and 4 (long-side edges).

resistance ( $R_c$ ), namely the additional resistance due to the contact between the carbonaceous trace and the metallic probes. Despite  $R_c$  is generally negligible for good conductors, in the case of LIG products its value might even be comparable to the sheet resistance [72].

### 3.6.1. Green LIG layers derived from neat wood (N-samples)

Samples N3-O, N4-O, N5-O showed comparable  $R_s$  values around  $100 \Omega/\text{sq}$ , suggesting that, once reached the activation of the substrate,

this system has few chances to be further optimized.

It has been demonstrated that the laser exposure of neat cellulose nanofibers in room conditions produces nearly exclusively amorphous carbon, graphitization occurring only after multiple lasing runs [53]. Therefore, it is reasonable to suppose that samples laser-scribed  $\perp$  to the wood grain (*i.e.* cellulose-rich direction) are characterized by a limited graphitization degree thanks to the synergic effect of aromatic and aliphatic wood components (see *paragraph 3.3*) [6,29,73].

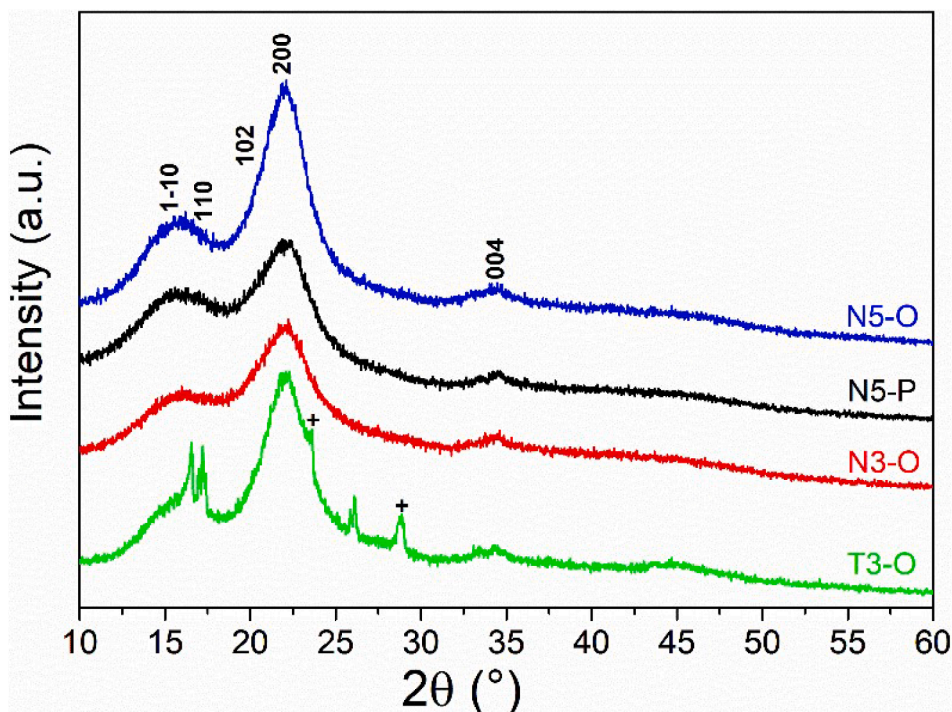


Fig. 13. XRD spectra of selected green LIG samples derived from neat wood (N5-O, N5-P, N3-O) and pretreated wood (T3-O).

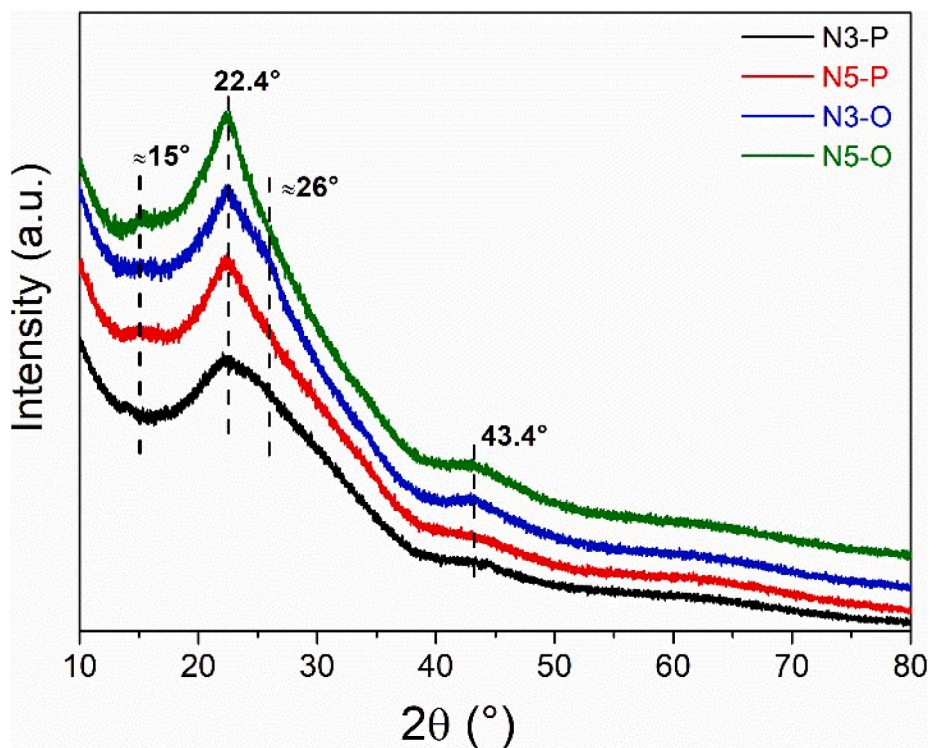


Fig. 14. XRD spectra of selected powdered derived from neat cedar wood: N3-P, N5-P, N3-O, N5-O.

The contained variation of the  $R_s$  values with the defocus off-set has to be attributed to the development of green LIG traces characterized by peculiar features in terms of microstructural architecture (Figs. 6a-d and 7a-b) and intrinsic structural properties (Table 2, Suppl. Fig. S1). Furthermore, the lasing  $\perp$  to the wood grain actually proceeds across several earlywood-to-latewood passages (*i.e.* growth rings) (Fig. 5a). On this basis, considering that earlywood and latewood tracheids exhibit

different features in terms of wood chemistry, ultrastructure and cell wall thickness (Fig. 2a) [24], it can be supposed that the limited impact of defocusing on the conductivity of N3-O, N4-O and N5-O has to be associated to the homogenization of local chemical and structural properties.

Regarding wood substrates laser-scribed  $\parallel$  to wood grain (*i.e.* lignin-rich direction), the  $R_s$  values of pristine wood ranged from tens of  $\Omega/\text{sq}$

**Table 3**  
Results of four-point-probe (FPP) measurements.

Sample	Sheet Resistance ( $R_s$ ) [ $\Omega/\text{sq}$ ]
N3-O	$134.9 \pm 0.2$
N4-O	$83.5 \pm 0.1$
N5-O	$102.9 \pm 0.1$
N3-P	$41.05 \pm 0.05$
N4-P	$86.3 \pm 0.1$
N5-P	$1925.0 \pm 0.7$
T3-O	$37.32 \pm 0.01$
T4-O	$130.33 \pm 0.02$
T5-O	$678.0 \pm 0.6$
T3-P	$329.1 \pm 0.1$
T4-P	$4972.8 \pm 0.3$
T5-P	$20,760 \pm 30$

to  $k\Omega/\text{sq}$  (Table 3), the lowest defocus off-set (i.e. -3 mm, sample N3-P) being the most favourable. It has been fully established that the key point for the conversion of lignocellulosic substrates in conductive layers is dominated by the efficiency of the graphitization process [6,74]. The mechanism is driven by the lignin content [29,32,37,38,74], prevalently located in compound middle lamella and cell corners [26–28, 73]. Therefore, it is reasonable to suppose that such process is favored when the laser writing runs along the lignin-rich direction (i.e. // to the wood grain). It is worth mentioning that the understanding of the structural evolution of lignin into multilayer graphene during direct laser writing presently remains still challenging [75].

Generally, the sheet resistance of single-step green LIG traces derived from pristine woods in room conditions and using a conventional laser source ranges from tens to thousands  $\Omega/\text{sq}$  [4,6,30]. It is worth mentioning that, despite higher costs and complexity, certain combinations of experimental conditions (e.g. operational laser parameters, multistep, irradiation atmosphere, pretreatments, embedded nanoparticles, bio-based inks), can lead to the conversion of various wood species in highly-conductive layers ( $R_s < 10 \Omega/\text{sq}$ ) [6,31,32,37].

Finally, the correlation between the electrical properties and defectiveness of graphite domains, deserve to be discussed. In fact, according to the data reported in Tables 2 and 3,  $R_s$  and  $I_D/I_G$  values collected for neat wood substrates followed an opposite trend (Suppl. Fig. S2). Such counterintuitive behaviour has been also reported by Lengger et al. [4] for green LIG traces derived from different pristine woods (e.g. plum tree and ebony) in similar experimental conditions. Interestingly, such effect seemed remarkably pronounced for samples obtained by lasing cedar wood in parallel to the wood grain (lignin-rich direction, //) (Suppl. Fig. S2).

Concluding, it can be deduced that the operative configuration that provides the minimum sheet resistance values also induces the highest defectiveness in the graphite domains, especially for wood substrates lased in // to the wood grain (i.e. lignin-rich direction) (Suppl. Fig. S2).

### 3.6.2. Green LIG layers derived from antifiame-treated wood (T-samples)

The electrical properties of T-samples are significantly affected by the laser scribing direction and defocusing, the  $R_s$  values spanning through three orders of magnitude (Table 3).

A valuable perspective is offered by the comparison between substrates laser-scribed along the  $\perp$  direction (T3-O, T4-O, T5-O) and in the // direction (T3-P, T4-P, T5-P). Interestingly, the two series show the same direct correlation of  $R_s$  with the defocusing off-set (Table 3). Then, the photo-thermal process that leads to the conversion of pretreated wood in conductive layers is again favoured when the distance of the substrates from the focal plane is minimized (i.e. -3 mm) whereas higher off-sets progressively encourage the simultaneous thermal decomposition of antifiame and/or residual by-products (Figs. 3, 7c-d) (paragraph 3.1). Moreover, the comparison between the electrical properties of T3-O and T3-P evidenced that the effectiveness of the antifiame is optimized when the laser scribing is performed orthogonally to the wood grain, the  $R_s$  values being, respectively, 37  $\Omega/\text{sq}$  and 329

$\Omega/\text{sq}$  (Table 3). Fully in line with both this trends, sample T5-P (i.e. // -scribed and highest defocusing off-set) is characterized by the highest sheet resistance value ( $R_s > 20,000 \Omega/\text{sq}$ ) (Figs. 6h-7d). Interestingly, T5-P also showed the highest  $I_D/I_G$  ratio compared to samples either lased at the same defocusing off-set (N5-O, N5-P and T5-O) or derived from pretreated substrates (T3-O, T4-O and T5-O).

Considering that cellulose nanofibers are the main the component of secondary cell walls they are more abundant along the direction orthogonal to the wood grain [22–25]. Therefore, taking in account their selective interaction with the phosphate-based antifiame (see paragraph 3.1), it can be supposed that  $\perp$ -scribed traces derived from pretreated wood substrates are favoured with respect to // -scribed ones thanks to the enhanced efficiency of the photothermal mechanisms that rules the onset of carbonization and graphitization (Fig. 4) [6,31,37,74].

Lastly, it has been observed that the exposure of the pretreated cedar wood to the laser source resulted in the formation of longitudinal defects oriented perpendicularly to the scribing path (Fig. 15) [31]. Such evidence occurred in all T-samples, independently from defocusing and direction of laser writing (Figs. 5d, 6g, 15c-d). Likely, the presence of these macroscopic flaws is due to the anisotropic ablation of the substrate as a consequence of the mismatch between the thermal properties of wood in the axial and transversal direction [76].

Then, the operative condition selected for the T-samples can be considered sub-optimal, especially in terms of writing speed that in this study has been fixed at 36 mm/s [31].

## 4. Conclusions

The wood of *Cedrus* sp. (cedar), a cultivation softwood widely diffused in the Mediterranean area, has been chosen as novel lignocellulosic substrate for green Laser Induced Graphitization aimed to the development of differential sensors, micro-fluidic cells and antennas for near-field communication within the paradigms of green electronics. These devices require sheet resistance ( $R_s$ ) values  $< 50 \Omega/\text{sq}$ . For such purpose, longitudinal wood specimen sub-radial oriented were selected and lased in room conditions employing a common laser source. Both pristine and antifiame pre-treated wood substrates were considered. Laser power (4–10 % max laser power 40 W), defocus off-set (-5 mm to 0 mm) and scribing direction (perpendicular or parallel to the wood grain) were systematically varied. A comprehensive characterization of green LIG products was carried out by optical microscopy (OM), thermogravimetry (TG), X-ray diffraction (XRD), scanning electron microscopy (SEM), photo-electron spectroscopy (XPS) and Raman spectroscopy. The electrical properties were investigated by 4-point probe (FPP) multi-meter.

The following concluding remarks can be drawn:

- Highly-interconnected 3D carbonaceous layers (thickness 150  $\mu\text{m}$ ), composed of  $sp^3$ -bonded carbons combined with amorphous  $sp^2$  carbon structures and high-defective graphitic regions (i.e.  $I_D/I_G$  2.79–1.25) have been obtained.
- Pretreatment of cedar wood with a commercial phosphate-based antifiame favored biochar formation and encouraged the graphitization process.
- Operative conditions that favor the graphitization of pristine cedar wood led to enhanced conductivity and increased defectiveness of graphite domains.
- Electrical properties of green LIG traces derived from cedar wood were remarkably affected by the lasing direction.
- The minimum value of sheet resistance was approximately 40  $\text{ohm}/\text{sq}$ , obtained for pristine wood substrates lased in parallel to the wood grain and for antifiame-treated wood lased perpendicularly to the wood grain.

Concluding, our study demonstrates that the lasing direction, usually ignored in previous investigations, is a key process parameter for the

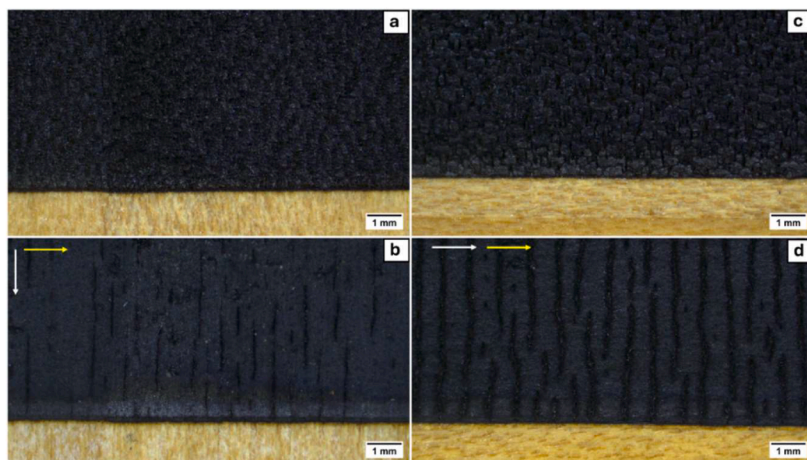


**Fig. 15.** Optical Microscopy (OM) of (a) N3-O, (b) T3-O, (c) N3-P and (d) T3-P (yellow arrow: laser-scribing direction; white arrow: wood grain direction).

fabrication of green LIG traces derived from softwood substrates.

Finally, it has to be underlined that, although green LIG technique has shown considerable success in small-scale devices such as electrodes and sensor probes, the transition to large antennas remains a challenging issue. Future wireless applications still require the achievement of multiple goals including minimize sheet resistance values to reach conductive properties suitable for long-range communication and enhance the durability of green LIG traces derived from wood through the development of specifically-designed strategies to protect the carbonaceous layers against mechanical and environmental deterioration.

Additionally, it is worth highlighting that the actual reproducibility of green LIG traces obtained with conventional laser equipment in room conditions can be a challenging issue. The conversion process of natural substrates into conductive carbonaceous layers is highly sensitive, not only to laser parameters and environmental variables, but also to local microstructural and compositional inhomogeneities intrinsic to lignocellulosic materials. Therefore, assessing the reproducibility of green LIG technique on wood substrates requires large-scale experimental campaigns and robust statistical analyses, that are beyond the scope of the present work and that will be addressed in future studies.

## Funding

This research did not receive any specific grant from funding agencies in the public, commercial, or not-for-profit sectors.

## CRedit authorship contribution statement

**Alessio Mostaccio:** Writing – review & editing, Writing – original draft, Methodology, Investigation, Data curation. **Francesco Bolognesi:** Writing – review & editing, Writing – original draft, Investigation. **Valerio Appetito:** Writing – original draft, Investigation. **Joanna Filippi:** Methodology, Investigation. **Leonardo Duranti:** Writing – review & editing, Writing – original draft, Visualization, Methodology, Investigation, Data curation. **Tilde De Caro:** Writing – original draft, Methodology, Investigation, Data curation. **Alessio Mezzi:** Writing – review & editing, Writing – original draft, Resources, Methodology, Investigation, Data curation. **Francesca Romana Lamastra:** Writing – review & editing, Writing – original draft, Visualization, Validation, Supervision. **Daniela Caschera:** Writing – review & editing, Writing – original draft, Supervision, Resources, Methodology, Investigation, Data curation. **Giampiero Montesperelli:** Writing – review & editing, Visualization, Supervision, Resources. **Eugenio Martinelli:** Writing – review & editing, Resources. **Marco Togni:** Writing – review & editing, Writing – original draft, Validation, Supervision, Resources, Conceptualization.

**Gaetano Marrocco:** Writing – review & editing, Writing – original draft, Validation, Supervision, Resources, Conceptualization. **Alessandra Bianco:** Writing – review & editing, Writing – original draft, Validation, Supervision, Resources, Methodology, Conceptualization.

## Declaration of competing interest

The authors declare that they have no known competing financial interests or personal relationships that could have appeared to influence the work reported in this paper.

## Supplementary materials

Supplementary material associated with this article can be found, in the online version, at [doi:10.1016/j.materresbull.2025.113460](https://doi.org/10.1016/j.materresbull.2025.113460).

## Data availability

No data was used for the research described in the article.

## References

- [1] W. Li, Q. Liu, Y. Zhang, C. Li, Z. He, W.C.H. Choy, P.J. Low, P. Sonar, A.K.K. Kyaw, Biodegradable materials and green processing for green electronics, *Adv. Mater* 32 (2020) e2001591, <https://doi.org/10.1002/adma.202001591>. Epub 2020 Jun 25. PMID: 32584502.
- [2] S. Imlimthan, P. Figueiredo, H.A. Santos, M. Sarparanta, Chapter 1 - Introduction to lignocellulosic materials, in: H. Santos, P. Figueiredo (Eds.), *Lignin-Based Materials for Biomedical Applications: Preparation, Characterization, and Implementation*, Elsevier, 2021, pp. 1–34, <https://doi.org/10.1016/B978-0-12-820303-3.00010-2>.
- [3] M. Titirici, S.G. Baird, T.D. Sparks, S.M. Yang, A. Brandt-Talbot, O. Hosseinaei, D. P. Harper, R.M. Parker, S. Vignolini, L.A. Berglund, Y. Li, H.L. Gao, L.B. Mao, S. H. Yu, N. Díez, G.A. Ferrero, M. Sevilla, P.Á. Szilágyi, C.J. Stubbs, P.A. Anderson, The sustainable materials roadmap, *J. Phys Mater.* 5 (2022), <https://doi.org/10.1088/2515-7639/ac4ee5>.
- [4] S.K. Lengger, L. Neumaier, L. Haiden, M. Feuchter, T. Griesser, J. Kosel, Laser-induced graphene formation on different wood species: dependence of electronic performance on intrinsic features of certain types of wood, *Sustain. Mater. Technol.* (2024) 40e00936, <https://doi.org/10.1016/j.susmat.2024.e00936>.
- [5] S. Bai, L. Ruan, H. Chen, Y. Du, H. Deng, N. Dai, Y. Tang, Laser-induced graphene: carbon precursors, fabrication mechanisms, material characteristics, and applications in energy storage, *Chem. Eng. J.* 493 (2024) 152805, <https://doi.org/10.1016/j.cej.2024.152805>.
- [6] P. Claro, T. Pinheiro, S. Silvestre, A. Marques, J. Coelho, J.M. Marconcin, E. Fortunato, L. Mattoso, R. Martins, Sustainable carbon sources for green laser-induced graphene: a perspective on fundamental principles, applications, and challenges, *Appl. Phys. Rev.* 9 (2022), <https://doi.org/10.1063/5.0100785>.
- [7] C.H. Dreimol, H. Guo, M. Ritter, T. Keplinger, Y. Ding, R. Günther, E. Poloni, I. Burgert, G. Panzarasa, Sustainable wood electronics by iron-catalyzed laser-induced graphitization for large-scale applications, *Nat. Commun.* 13 (2022), <https://doi.org/10.1038/s41467-022-31283-7>.

- [8] A. Mostaccio, G. Marrocco, Laser-induced graphene: a green technology for the IoT, *IEEE Electron Devices Mag.* 2 (2024) 11–22, <https://doi.org/10.1109/MED.2024.3376243>.
- [9] Y. Chyan, R. Ye, Y. Li, S.P. Singh, C.J. Arnusch, J.M. Tour, Laser-induced graphene by multiple lasing: toward electronics on cloth, paper, and food, *ACS Nano* 12 (2018) 2176–2183, <https://doi.org/10.1021/acsnano.7b08539>.
- [10] H.K. Nam, T.S.D. Le, D. Yang, B. Kim, Y. Lee, J.S. Hwang, Y.R. Kim, H. Yoon, S. W. Kim, Y.J. Kim, Smart wooden home enabled by direct-written laser-induced graphene, *Adv. Mater. Technol.* 8 (2023) 2201952, <https://doi.org/10.1002/admt.202201952>.
- [11] J. Zhu, S. Liu, Z. Hu, X. Zhang, N. Yi, K. Tang, M.G. Dexheimer, X. Lian, Q. Wang, J. Yang, J. Gray, H. Cheng, Laser-induced graphene non-enzymatic glucose sensors for on-body measurements, *Biosens. Bioelectron.* 193 (2021), <https://doi.org/10.1016/j.bios.2021.113606>.
- [12] G.S. Wilson, Y. Hu, Enzyme-based biosensors for *in vivo* measurements, *Chem. Rev* 100 (2000) 2693–2704, <https://doi.org/10.1021/cr990003y>.
- [13] P. Puetz, A. Behrent, A.J. Baeumner, J. Wegener, Laser-scribed graphene (LSG) as new electrode material for impedance-based cellular assays, *Sens. Actuators B Chem.* 321 (2020), <https://doi.org/10.1016/j.snb.2020.128443>.
- [14] Z. Wan, M. Umer, M. Lobino, D. Thiel, N.-T. Nguyen, A. Trinchì, M.J.A. Shiddiky, Y. Gao, Q. Li, Laser induced self-N-doped porous graphene as an electrochemical biosensor for femtomolar miRNA detection, *Carbon* 163 (2020) 385–394, <https://doi.org/10.1016/j.carbon.2020.03.043>.
- [15] M. Bahri, M.A. Elaguech, S. Nasraoui, K. Djebbi, O. Kanoun, P. Qin, C. Tlili, D. Wang, Laser-Induced graphene electrodes for highly sensitive detection of DNA hybridization via consecutive cytosines (polyC)-DNA-based electrochemical biosensors, *Microchim. J.* 185 (2023), <https://doi.org/10.1016/j.microc.2022.108208>.
- [16] J. Gao, S. He, A. Nag, J.W.C. Wong, A review of the use of carbon nanotubes and graphene-based sensors for the detection of aflatoxin M1 compounds in milk, *Sensors* 21 (2021) 3602, <https://doi.org/10.3390/s21113602>.
- [17] Y. Yang, Y. Song, X. Bo, J. Min, O.S. Pak, L. Zhu, M. Wang, J. Tu, A. Kogan, H. Zhang, T.K. Hsiai, Z. Li, W. Gao, A laser-engraved wearable sensor for sensitive detection of uric acid and tyrosine in sweat, *Nat. Biotechnol.* 38 (2020) 217–224, <https://doi.org/10.1038/s41587-019-0321-x>.
- [18] J. Liu, H. Ji, X. Lv, C. Zeng, H. Li, F. Li, B. Qu, F. Cui, Q. Zhou, Laser-induced graphene (LIG)-driven medical sensors for health monitoring and diseases diagnosis, *Microchim. Acta* 189 (2022), <https://doi.org/10.1007/s00604-021-05157-6>.
- [19] M.D. Wagh, S.K. Sahoo, S. Goel, Laser-induced graphene ablated polymeric microfluidic device with interdigital electrodes for taste sensing application, *Sens. Actuators A Phys.* 333 (2022), <https://doi.org/10.1016/j.sna.2021.113301>.
- [20] T.D. Le, Y.A. Lee, H.K. Nam, K.Y. Jang, D. Yang, B. Kim, K. Yim, S. Kim, H. Yoon, Y. Kim, Green flexible graphene–inorganic hybrid micro supercapacitors made of fallen leaves enabled by ultrafast laser pulses, *Adv. Funct. Mater.* 32 (2022), <https://doi.org/10.1002/adfm.202107768>.
- [21] H. Huang, S. Su, N. Wu, H. Wan, S. Wan, H. Bi, L. Sun, Graphene-based sensors for human health monitoring, *Front. Chem.* 7 (2019), <https://doi.org/10.3389/fchem.2019.00399>.
- [22] C. Chen, Y. Kuang, S. Zhu, et al., Structure–property–function relationships of natural and engineered wood, *Nat. Rev. Mater.* 5 (2020) 642–666, <https://doi.org/10.1038/s41578-020-0195-z>.
- [23] E. Hågglund, *Chemistry of Wood*, Academic Press, New York, N. Y., 1951.
- [24] E. Sjöström, *Wood Chemistry: Fundamentals and Applications*, 2nd ed., Elsevier, 1993 <https://doi.org/10.1016/C2009-0-03289-9>.
- [25] A. Kumar, T. Jyske, M. Petrić, Delignified wood from understanding the hierarchically aligned cellulose structures to creating novel functional materials: a review, *Adv. Sustain. Syst.* 5 (5) (2021) 2000251, <https://doi.org/10.1002/advs.202000251>.
- [26] J. Fromm, B. Rockel, S. Lautner, E. Windeisen, G. Wanner, Lignin distribution in wood cell walls determined by TEM and backscattered SEM techniques, *J. Struct. Biol* 143 (2003) 77–84, [https://doi.org/10.1016/S1047-8477\(03\)00119-9](https://doi.org/10.1016/S1047-8477(03)00119-9).
- [27] Y. Zhang, M. Naebe, Lignin: a review on structure, properties, and applications as a light-colored UV absorber, *ACS Sustain. Chem. Eng.* 9 (2021) 1427–1442, <https://doi.org/10.1021/acsschemeng.0c06998>.
- [28] M. Takada, R. Chandra, J. Wu, J.N. Saddler, The influence of lignin on the effectiveness of using a chemo-thermomechanical pulping-based process to pretreat softwood chips and pellets prior to enzymatic hydrolysis, in: *Bioresource Technology*, 302, Elsevier Ltd, 2020, <https://doi.org/10.1016/j.biortech.2020.122895>.
- [29] R. Ye, Y. Chyan, J. Zhang, Y. Li, X. Han, C. Kittrell, J.M. Tour, Laser-induced graphene formation on wood, *Adv. Mater.* 29 (2017) 1702211, <https://doi.org/10.1002/adma.201702211>.
- [30] C. Qu, M. Lu, Z. Zhang, S. Chen, D. Liu, D. Zhang, J. Wang, B. Sheng, Flexible microstructured capacitive pressure sensors using laser engraving and graphitization from natural wood, *Molecules* 28 (2023) 5339, <https://doi.org/10.3390/molecules28145339>.
- [31] T.-S.D. Le, S. Park, J. An, P.S. Lee, Y.-J. Kim, Ultrafast laser pulses enable one-step graphene patterning on woods and leaves for green electronics, *Adv. Funct. Mater.* 29 (2019) 1902771, <https://doi.org/10.1002/adfm.201902771>.
- [32] X. Han, R. Ye, Y. Chyan, T. Wang, C. Zhang, L. Shi, T. Zhang, Y. Zhao, J.M. Tour, Laser-induced graphene from wood impregnated with metal salts and use in electrocatalysis, *ACS Appl. Nano Mater.* 1 (2018) 5053–5061, <https://doi.org/10.1021/acsnanm.8b01163>.
- [33] P.M. Pijut, The True Cedars, *Arboric. Urban For.* 26 (2000) 218–224, <https://doi.org/10.48044/jauf.2000.026>.
- [34] E. Fusaro, *Caratteristiche e distribuzione dei rimboschimenti di cedro in Italia*, *Cellul. Carta* 42 (1991) 17–24.
- [35] S. Mohan, A. Pal, R. Singh, Biodiesel production from *Cedrus deodara* oil in different types of ultrasonic reactors and energy analysis, *Energy Sources A Recovery Util. Environ. Eff.* 38 (2016) 3709–3715, <https://doi.org/10.1080/15567036.2016.1141271>.
- [36] M. Güleç, S.A. Kiremitci, O. Abdullah, *Cedrus Libani* A. Rich, in: F.T. Güragaç Dereli, M. İlhan, T. Belwal (Eds.), *Novel Drug Targets With Traditional Herbal Medicines*, Springer International Publishing, 2022, pp. 109–119, [https://doi.org/10.1007/978-3-031-07753-1\\_8](https://doi.org/10.1007/978-3-031-07753-1_8).
- [37] A.C. Bressi, A. Dallinger, Y. Steksova, F. Greco, Bioderived laser-induced graphene for sensors and supercapacitors, *ACS Appl. Mater. Interfaces* 15 (2023) 35788–35814, <https://doi.org/10.1021/acami.3c07687>.
- [38] J. Edberg, R. Brooke, O. Hosseinaei, et al., Laser-induced graphitization of a forest-based ink for use in flexible and printed electronics, *npj Flex Electron* 4 (2020) 17, <https://doi.org/10.1038/s41528-020-0080-2>.
- [39] F.M. Smits, Measurement of sheet resistivities with the four-point probe, *Bell Syst. Tech. J.* 37 (1958), <https://doi.org/10.1002/j.1538-7305.1958.tb03883.x>.
- [40] H. Topsoe, Geometric factors in four-point resistivity measurement, *Bulletin* 472 (1968).
- [41] E.E. Thybring, M. Fredriksson, Wood modifications as a tool to understand moisture in wood, *Forests* 12 (2021) 372, <https://doi.org/10.3390/f12030372>.
- [42] Forest Products Laboratory, General Technical Report FPL-GTR-282, U.S. Department of Agriculture, Forest Service, Forest Products Laboratory, Madison, WI, 2021, p. 543. ISBN 9798846323247, <https://research.fs.usda.gov/treesearch/62200>.
- [43] A. Chaparadza, S. Majoni, The effects of aluminum and silicon phosphates on thermal stability and flammability of polystyrene, *J. Chem. Sci.* 134 (2022), <https://doi.org/10.1007/s12039-021-02006-0>.
- [44] A.D. French, Idealized powder diffraction patterns for cellulose Polymorphs, *Cellulose* 21 (2014) 885–896, <https://doi.org/10.1007/s10570-013-0030-4>.
- [45] M. Poletto, A.J. Zattera, M.M. Forte, R.M. Santana, Thermal decomposition of wood: influence of wood components and cellulose crystallite size, *Bioresour. Technol.* 109 (2012) 148–153, <https://doi.org/10.1016/j.biortech.2011.11.122>.
- [46] S. Sinha, A. Jhalani, M.R. Ravi, R. Anjan, Modeling of pyrolysis in wood: a review, *J. Sol. Energy Soc. India* 10 (2000) 41–62.
- [47] F. Bolognesi, L. Duranti, V. Bertolini, A. Bianco, F.R. Lamastra, M. Togni, B. Alessandra, Cellulose-rich templates from naturally found and cultivation woods diffused in the South-European area: a comprehensive investigation for novel wood-polymer hybrids, *Cellulose* (2024), <https://doi.org/10.1007/s10570-024-06210-2> press.
- [48] A.F. Roberts, The heat of reaction during the pyrolysis of wood, *Combust. Flame* 17 (1971) 79–86.
- [49] O. Grexa, E. Horvathova, O. Besinova, P. Lehocky, Flame retardant treated plywood, *Polym. Degrad. Stab.* 64 (1999) 529–533.
- [50] A. Sheikh, K.G. Rewatkar, XRD, EDX and thermal analysis of glycine-doped ammonium dihydrogen phosphate crystal, in: *AIP Conf. Proc.* 2104, 2019 030036, <https://doi.org/10.1063/1.5100463>.
- [51] A. Marcilla, M.I. Beltran, A. Gómez-Siurana, I. Martínez-Castellanos, D. Berenguer, V. Pastor, A.N. García, TGA/FTIR study of the pyrolysis of diammonium hydrogen phosphate–tobacco mixtures, *J. Anal. Appl. Pyrolysis* 112 (2015) 48–55, <https://doi.org/10.1016/j.jaap.2015.02.023>.
- [52] A. Mezzi, S. Kaciulis, Surface investigation of carbon films: from diamond to graphite, *Surf. Interface Anal.* 42 (2010) 1082, <https://doi.org/10.1002/sia.3348>.
- [53] S. Lee, S. Jeon, Laser-induced graphitization of cellulose nanofiber substrates under ambient conditions, *ACS Sustain. Chem. Eng.* 7 (2019) 2270–2275, <https://doi.org/10.1021/acssuschemeng.8b04955>.
- [54] V. Thapliyal, M.E. Alabdulkarim, D.R. Whelan, B. Mainali, J.L. Maxwell, A concise review of the Raman spectra of carbon allotropes, *Diam. Relat. Mater.* 127 (2022) 109180, <https://doi.org/10.1016/j.diamond.2022.109180>.
- [55] J. Ji, S. Dong, A. Zhang, Q. Zhang, Low-frequency interlayer vibration modes in two-dimensional layered materials, *Phys. E Low-Dimens. Syst. Nanostruct.* 80 (2016) 130–141, <https://doi.org/10.1016/j.physe.2016.01.040>.
- [56] C.C. Zhang, S. Hartlaub, I. Petrovic, B. Yilmaz, Raman spectroscopy characterization of amorphous coke generated in industrial processes, *ACS Omega* 7 (2022) 2565–2570, <https://doi.org/10.1021/acsomega.1c03456>.
- [57] A. Dubale, W.-N. Su, A. Gedamu Tamirat, C.-J. Pan, B.A. Aragaw, H.-M. Chen, C.-H. Chen, B.J. Hwang, The synergetic effect of graphene on Cu<sub>2</sub>O nanowire arrays as a highly efficient hydrogen evolution photocathode in water splitting, *J. Mater. Chem.* 2 (2014) 18383–18397, <https://doi.org/10.1039/c4ta03464c>.
- [58] A. Inam, R. Brydson, D.V. Edmonds, Raman spectroscopy study of the crystallinity of graphite formed in an experimental free machining steel, *Mater. Charact.* 163 (2020) 110264, <https://doi.org/10.1016/j.matchar.2020.110264>.
- [59] F. Mori, M. Kubouchi, Y. Arao, Effect of graphite structures on the productivity and quality of few-layer graphene in liquid-phase exfoliation, *J. Mater. Sci.* 53 (2018) 12807–12815, <https://doi.org/10.1007/s10853-018-2538-3>.
- [60] F. Tuinstra, J.L. Koenig, Raman spectrum of graphite, *J. Chem. Phys.* 53 (1970) 1126–1130, <https://doi.org/10.1063/1.1674108>.
- [61] L.G. Cañado, K. Takai, T. Enoki, M. Endo, Y.A. Kim, et al., General equation for the determination of the crystallite size La of nanographite by Raman spectroscopy, *Appl. Phys. Lett.* 88 (2006) 163106, <https://doi.org/10.1063/1.2196057>.
- [62] A. Merlen, J.G. Buijnsters, C.A. Pardanaud, Guide to and review of the use of multi-wavelength Raman spectroscopy for characterizing defective aromatic carbon solids: from graphene to amorphous carbons, *Coatings* 7 (2017) 153, <https://doi.org/10.3390/coatings7100153>.

- [63] A.C. Ferrari, Raman spectroscopy of graphene and graphite: disorder, electron–phonon coupling, doping and non-adiabatic effects, *Solid State Commun.* 143 (2007) 47–57, <https://doi.org/10.1016/j.ssc.2007.03.052>.
- [64] D. Schüpfer, F. Badaczewski, J. Guerra-Castro, D. Hofmann, C. Heiliger, B. Smarsly, P. Klar, Assessing the structural properties of graphitic and non-graphitic carbons by Raman spectroscopy, *Carbon* 161 (2020), <https://doi.org/10.1016/j.carbon.2019.12.094>.
- [65] O. Frank, M. Mohr, J. Maultzsch, C. Thomsen, I. Riaz, R. Jalil, K.S. Novoselov, G. Tsoukleri, J. Parthenios, K. Papagelis, L. Kavan, C. Galiotis, Raman 2D-band splitting in graphene: theory and experiment, *ACS Nano* 5 (2011) 2231–2239, <https://doi.org/10.1021/nn103493g>.
- [66] Y. Katsuyama, Y. Nakayasu, K. Oizumi, Y. Fujihara, H. Kobayashi, I. Honma, Quinone-based redox supercapacitor using highly conductive hard carbon derived from Oak wood, *Adv. Sustain. Syst.* 3 (2019), <https://doi.org/10.1002/advsu.201900083>.
- [67] A. Mostaccio, G. Antonelli, M. Bragaglia, E. Martinelli, G. Marrocco, Comparative evaluation of laser-induced graphene (LIG) traces on polyimide under soft and hard stress for IoT applications, *IEEE J. Flex. Electron.* 2 (2023), <https://doi.org/10.1109/jflex.2023.3265356>.
- [68] P. Zaccagnini, A. Lamberti, A perspective on laser-induced graphene for micro-supercapacitor application, *Appl. Phys. Lett.* 120 (2022) 100501, <https://doi.org/10.1063/5.0078707>.
- [69] M.G. Stanford, K. Yang, Y. Chyan, C. Kittrell, J.M. Tour, Laser-induced graphene for flexible and embeddable gas sensors, *ACS Nano* 13 (2019) 3474–3482, <https://doi.org/10.1021/acsnano.8b09622>.
- [70] A.F. Carvalho, A.J.S. Fernandes, C. Leitão, J. Deurmeier, A.C. Marques, R. Martins, E. Fortunato, F.M. Costa, Laser-induced graphene strain sensors produced by ultraviolet irradiation of polyimide, *Adv. Funct. Mater.* 28 (2018) 1805271, <https://doi.org/10.1002/adfm.201805271>.
- [71] J. De la Roche, I. López-Cifuentes, A. Jaramillo-Botero, Influence of lasing parameters on the morphology and electrical resistance of polyimide-based laser-induced graphene (LIG), *Carbon Lett.* 33 (2023) 587–595, <https://doi.org/10.1007/s42823-022-00447-2>.
- [72] S. Russo, M.F. Craciun, M. Yamamoto, A.F. Morpurgo, S. Tarucha, Contact resistance in graphene-based devices, *Phys. Low Dimen. Syst. Nanostruct.* 42 (2010), <https://doi.org/10.1016/j.physe.2009.11.080>.
- [73] A. Tribot, G. Amer, M. Abdou Alio, H. deBaynast, C. Delattre, A. Pons, J.-D. Mathias, J.-M. Callois, C. Vial, P. Michaud, C.-G. Dussap, Wood-lignin: supply, extraction processes and use as bio-based material, *Eur. Polym. J.* 112 (2019) 228–240, <https://doi.org/10.1016/j.eurpolymj.2019.01.007>.
- [74] T.S.D. Le, H.P. Phan, S. Kwon, S. Park, Y. Jung, J. Min, B.J. Chun, H. Yoon, S.H. Ko, S.W. Kim, Y.J. Kim, Recent advances in laser-induced graphene: mechanism, fabrication, properties, and applications in flexible electronics, *Adv. Funct. Mater.* 32 (48) (2022) 2205158, <https://doi.org/10.1002/adfm.202205158>.
- [75] H. Zhang, Q. Li, K.D. Hammond, X. He, J. Lin, C. Wan, Probing laser-induced structural transformation of lignin into few-layer graphene, *Green Chem.* 26 (2024) 5921–5932, <https://doi.org/10.1039/D3GC03603K>.
- [76] G. Goli, F. Becherini, M.C. Di Tuccio, A. Bernardi, M. Fioravanti, Thermal expansion of wood at different equilibrium moisture contents, *J. Wood Sci.* 65 (2019) 4, <https://doi.org/10.1186/s10086-019-1781-9>.